

A Stochastic Conceptual Model for the Coupled ENSO and MJO

Charlotte Moser¹, Nan Chen^{1,*}, and Yinling Zhang¹

¹Department of Mathematics, University of Wisconsin–Madison, Madison, WI 53706, USA

*Corresponding author: Nan Chen, chenan@math.wisc.edu

November 11, 2024

Summary

Understanding the interactions between the El Niño-Southern Oscillation (ENSO) and the Madden-Julian Oscillation (MJO) is essential to studying climate variabilities and predicting extreme weather events. Here, we develop a stochastic conceptual model for describing the coupled ENSO-MJO phenomenon. The model adopts a three-box representation of the interannual ocean component to characterize the ENSO diversity. For the intraseasonal atmospheric component, a low-order Fourier representation is used to describe the eastward propagation of the MJO. We incorporate decadal variability to account for modulations in the background state that influence the predominant types of El Niño events. In addition to dynamical coupling through wind forcing and latent heat, state-dependent noise is introduced to characterize the statistical interactions among these multiscale processes, improving the simulation of extreme events. The model successfully reproduces the observed non-Gaussian statistics of ENSO diversity and MJO spectra. It also captures the interactions between wind, MJO, and ENSO.

1 Introduction

The El Niño-Southern Oscillation (ENSO) is one of the most significant interannual climate phenomena in the equatorial Pacific, exerting a strong influence on global weather and climate patterns (Ropelewski and Halpert, 1987, McPhaden et al., 2006a, Latif et al., 1998, Neelin et al., 1998). ENSO is characterized by quasi-regular cycles in sea surface temperature (SST) across the central and eastern Pacific. ENSO has two phases: El Niño and La Niña, which correspond to positive and negative SST anomalies, respectively. Recent studies have highlighted the diversity and complexity of ENSO (Capotondi et al., 2015, Timmermann et al., 2018). ENSO diversity indicates at least two distinct types of El Niño: the eastern Pacific (EP) and central Pacific (CP) events (Ashok et al., 2007, Kao and Yu, 2009, Kim et al., 2012). The peak SST anomalies occur in different regions for each type, with EP events centered in the cold tongue region and CP events near the dateline (Larkin and Harrison, 2005, Yu and Kao, 2007, Ashok et al., 2007, Kao and Yu, 2009, Kug et al., 2009). ENSO complexity further encompasses a range of features, including variations in spatial patterns, peak intensity, and temporal evolution, underscoring the intricate nature of the interannual phenomenon (Chen and Cane, 2008, Jin et al., 2008, Barnston et al., 2012, Hu et al., 2012, Zheng et al., 2014, Fang et al., 2015, Sohn et al., 2016, Santoso et al., 2019). Notably, ENSO was identified as a product of tropical air-sea interaction back in the 1960s (Bjerknes, 1969). Since then, coupled atmosphere and ocean systems have been widely used to improve the understanding of the ENSO.

The Madden-Julian Oscillation (MJO) is a prominent intraseasonal climate pattern characterized by large-scale fluctuations in tropical rainfall and atmospheric circulation (Zhang, 2005, Woolnough, 2019, Zhang et al., 2020). The MJO has been observed to have a significant impact on the ENSO (Tang and Yu, 2008, McPhaden et al., 2006b, Hendon et al., 2007). The MJO and the convectively-coupled Rossby waves modulate westerly and easterly wind events (Puy et al., 2016, 2019). Therefore, they enhance or suppress the development of El Niño and La Niña events by altering wind patterns and convection over the Pacific Ocean (Jauregui and Chen, 2024, Harrison and Vecchi, 1997, Vecchi and Harrison, 2000, Tziperman and Yu, 2007). Conversely, the SST anomalies, which influence convection and precipitation, affect the amplitude, duration, and spatiotemporal patterns of the MJO (Moon et al., 2011, Lee et al.,

2019). Understanding the interactions between ENSO and MJO facilitates the study of climate variability and improves the forecast of extreme events.

The interaction between the MJO and ENSO is increasingly recognized in climate models, where incorporating this relationship improves both the understanding of model physics and forecast accuracy (Mengist and Seo, 2022, Liu et al., 2017, Ahn et al., 2017, Hung et al., 2013, Fernandes and Grimm, 2023). Significant progress has been made in recent years toward more realistic simulations of the MJO and ENSO in climate models (Khouider et al., 2011, Ajayamohan et al., 2013, Guilyardi et al., 2020, Capotondi et al., 2020). However, fully capturing the complexities of ENSO, MJO, and their interactions in operational models remains a challenge. Many models in the Coupled Model Intercomparison Project (CMIP), for example, struggle to accurately simulate ENSO diversity, particularly CP events and the strong non-Gaussian characteristics in SST statistics (Chen et al., 2017, Dieppois et al., 2021, Capotondi, 2013, Atwood et al., 2017). Such model errors often lead to the underestimation of ENSO teleconnections (Jiang et al., 2021, Li et al., 2019, Fang et al., 2024a). Similarly, biases in simulating background atmospheric conditions continue to hinder the accurate representation of the MJO in several operational models (Kim, 2017, Chen et al., 2022a).

Conceptual models are valuable tools for breaking down complex phenomena into fundamental components, helping to clarify mechanisms such as feedback loops and interactions between different elements. They also improve the simulation of large-scale features. Insights from conceptual models guide the development of more advanced models, while their accurate simulations and statistics enhance the simulations from more complicated models through multi-model data assimilation and reanalysis (Parsons et al., 2021, Bach and Ghil, 2023, Chen and Stechmann, 2019). Since the 1980s, various low-dimensional conceptual models have been developed to describe the basic oscillatory behavior of traditional ENSO (Jin, 1997, Schopf and Suarez, 1988, Wang et al., 2017, Wang and Picaut, 2004, McCreary, 1983, Weisberg and Wang, 1997, Picaut et al., 1996, Wang, 2001, Chen and Zhang, 2023). More recently, several new conceptual models based on the recharge oscillator framework have emerged to capture ENSO diversity (Chen et al., 2022b, Geng et al., 2020, Fang et al., 2024b). These models have been used to study the predictability of ENSO's large-scale patterns (Fang and Chen, 2023) and to analyze the statistical response to perturbations in initial conditions and model parameters (Andreou and Chen, 2024). Their statistically accurate outputs have also served as training datasets for machine learning approaches aimed at uncovering critical physical processes (Zhang et al., 2024). Furthermore, these conceptual models have been used as foundational building blocks for developing simple or intermediate-coupled models (ICMs) (Zebiak and Cane, 1987, Geng and Jin, 2022, 2023, Chen and Fang, 2023, Thual et al., 2016). However, the atmospheric components in the existing conceptual models are highly parameterized, and the explicit coupling between the MJO and ENSO has not been adequately addressed in most existing conceptual models. Developing a coupled ENSO-MJO conceptual model would not only bring new insights into natural processes but also facilitate the study of ENSO dynamics, as was highlighted in a recent ENSO recharge oscillator review paper (Vialard, 2024).

In this paper, a stochastic conceptual model is developed to describe the coupled MJO and ENSO phenomena. The ENSO component is represented by a three-box model spanning the equatorial Pacific, capturing large-scale interannual variability across the western Pacific (WP), CP, and EP regions. The model specifically focuses on the CP and EP SSTs, which are critical variables for capturing the diversity and complexity of ENSO events (Chen et al., 2022b). For the atmospheric component, a stochastic skeleton model (Thual et al., 2014) is utilized as the building block, which has been shown to reproduce many of the observed MJO features. Rather than using a box model, the MJO dynamics in this conceptual model is represented by the leading three Fourier modes from the skeleton model, allowing for a more accurate representation of the eastward propagation of its large-scale features. The coupling between the atmosphere and ocean is modeled such that wind bursts drive ocean currents, while latent heat flux from the ocean influences the strength of convective activity and moisture in the atmosphere. State-dependent noise is incorporated to more effectively capture the feedback mechanisms from the ocean to the atmosphere. The state-dependent noise is crucial for the model to reproduce the observed non-Gaussian statistics. Finally, a decadal variable is introduced into the coupled conceptual model to modulate the background state (Capotondi et al., 2023, Power et al., 2021), allowing the model to favor either CP or EP El Niño events with varying frequency over time.

The rest of the paper is organized as follows. Section 2 provides a detailed description of the model. Section 3 outlines the datasets used in this research. The simulation results and corresponding statistical analysis of the coupled model are presented in Section 4. The paper

is concluded in Section 5.

2 The Model

The coupled ENSO-MJO model comprises an interannual ocean component, two atmospheric components (intraseasonal and interannual), and a decadal variability. ENSO is represented by SST variables in the ocean model, while the MJO is reconstructed from a linear combination of the intraseasonal atmospheric variables.

2.1 Interannual ocean model

The interannual ocean model (2.1) is a generalized extension of the classical recharge oscillator model (Jin, 1997), applied over the WP, CP and EP to capture both types of ENSO events and their diversity (Chen et al., 2022b). This model incorporates the ocean’s heat content discharge-recharge processes and zonal advection. In the model, T_C and T_E represent the SST anomalies in the CP and EP, respectively, U denotes the zonal ocean current in the CP, and h_W corresponds to the thermocline depth in the WP. The model reads:

$$\frac{dU}{dt} = -rU - \frac{\alpha_1 b_0 \mu}{2} (T_C + T_E) + \beta_u(I)\tau, \quad (2.1a)$$

$$\frac{dh_W}{dt} = -rh_W - \frac{\alpha_2 b_0 \mu}{2} (T_C + T_E) + \beta_h(I)\tau, \quad (2.1b)$$

$$\frac{dT_C}{dt} = \left(\frac{\gamma b_0 \mu}{2} - c_1(T_C, t) \right) T_C + \frac{\gamma b_0 \mu}{2} T_E + \gamma h_W + \rho IU + C_U + \beta_C(I)\tau, \quad (2.1c)$$

$$\frac{dT_E}{dt} = \gamma h_W + \left(\frac{3\gamma b_0 \mu}{2} - c_2(t) \right) T_E - \frac{\gamma b_0 \mu}{2} T_C + \beta_E(I)\tau. \quad (2.1d)$$

Two additional variables appear in the interannual ocean model, which will be discussed in the following subsections. The first is the decadal variable I , appearing in (2.1c). This variable accounts for the long-term modulation of Walker circulation’s influence on ENSO, allowing the model to favor the development of either EP or CP events. It also represents the zonal SST gradient between the WP and CP, affecting interannual variability by modulating the efficiency of zonal advection through the IU term. The second key variable is τ , which represents atmospheric wind in the WP region and incorporates both intraseasonal and interannual components. In addition, the influence of seasonality has been incorporated into the two damping coefficients, c_1 and c_2 , to more accurately capture the seasonal phase-locking behavior of ENSO. This behavior is characterized by the tendency of ENSO events to peak during boreal winter (Tziperman et al., 1997, Stein et al., 2014, Fang and Zheng, 2021).

It is worth explaining the model mechanisms for triggering CP and EP El Niño events. In the absence of the stochastic wind forcing, the model is a deterministic and nearly linear system if the decadal variable I is held constant. Note that there is a non-linearity in the damping term of (2.1c), but it is weak and does not play a significant role when examining the function of the strong non-linear term IU . The model exhibits different oscillatory patterns depending on the fixed value of I (Fang and Mu, 2018). When I is small, corresponding to weak advection, the model generates an EP El Niño cycle. In contrast, when I is large, the strengthened Walker circulation enhances the role of advection, leading to a dominant CP El Niño oscillatory pattern. The time-varying I , combined with the stochastic forcing, allows for the occurrence of different El Niño events over time. Depending on the value of I , one type of event becomes more likely during a given period, thereby reproducing the observed alternation between EP- and CP-dominant phases (Yu and Kim, 2013).

2.2 Decadal variability

The decadal variability in the conceptual model is primarily used to modulate the background state over the equatorial Pacific (Capotondi et al., 2023, Power et al., 2021), favoring the generation of more EP or CP events over specific time periods. Developing a comprehensive model describing the decadal variation is not the main focus. To this end, a simple linear stochastic process is employed as the governing equation for the decadal variable I ,

$$\frac{dI}{dt} = -\lambda(I - \bar{I}) + \sigma_I(I)\dot{W}_I, \quad (2.2)$$

where the damping coefficient λ is chosen such that I varies in the decadal timescale and \bar{I} is the mean state. It is important to note that the trade winds in the lower level of the Walker circulation on decadal timescales are predominantly easterly. This implies that the sign of I remains constant over time, resulting in a non-Gaussian distribution of I . This feature can be easily integrated into the linear stochastic process of I by using a state-dependent noise coefficient (Averina and Artemiev, 1988, Yang et al., 2021). Given the limited observational data and the principle of deriving the least biased maximum entropy solution for a distribution (Chen, 2023), a uniform distribution is adopted for I in this work. Here, a larger value of I corresponds to stronger easterly trade winds.

2.3 Intraseasonal atmosphere model

The intraseasonal model generates intraseasonal wind, a key trigger for El Niño events. Unlike prior studies that used a single process or noise to represent wind in ENSO models (Chen et al., 2022b, Geng et al., 2020, Jin et al., 2007), this model employs simple atmospheric equations to capture more detailed dynamics, including the MJO. This allows for studying MJO-ENSO coupling.

The governing equations are based on the stochastic skeleton model for the MJO (Thual et al., 2014). However, only the modes up to the third zonal wavenumber are retained, simplifying the model while still capturing large-scale MJO features (Majda and Stechmann, 2009, 2011, Ling et al., 2017). The governing equations, written in terms of Fourier modes, are as follows,

$$\frac{d\hat{K}_k}{dt} = -d_k\hat{K}_k - ik\hat{K}_k - \bar{H}\hat{A}_k/2, \quad (2.3a)$$

$$\frac{d\hat{R}_k}{dt} = -d_k\hat{R}_k + ik\hat{R}_k/3 - \bar{H}\hat{A}_k/3, \quad (2.3b)$$

$$\frac{d\hat{Q}_k}{dt} = -d_k\hat{Q}_k - ik\bar{Q}(\hat{K}_k - \hat{R}_k/3) + \bar{H}\hat{A}_k(\bar{Q}/6 - 1) + \sigma_{\hat{Q}_k}(E_q)\dot{W}_{\hat{Q}_k}, \quad (2.3c)$$

$$\frac{d\hat{A}_k}{dt} = -\lambda_A\hat{A}_k + \sum_j \Gamma\hat{Q}_j(\hat{A}_{k-j} + \bar{A}_{k-j}) + \sigma_{\hat{A}_k}(Q, A)\dot{W}_{\hat{A}_k}, \quad (2.3d)$$

where $k = 0, \pm 1, \pm 2$ and ± 3 . The four model variables (indicated with hats) on the left-hand side of (2.3) are the Fourier coefficients of the Kelvin wave (K), Rossby wave (R), moisture (Q), and convective activity (A), which are all anomalies. Note that \bar{A}_k represents the Fourier coefficients of \bar{A} , which is the background convective activity computed by

$$H\bar{A} = E_q + S^q - \bar{Q}S^\theta/(1 - \bar{Q}), \quad (2.4)$$

where S^θ and S^q are the external source of cooling and moistening, respectively. Both S^θ and S^q are pre-determined, peaking in the warm pool region. In (2.4), E_q is the latent heat that is affected by the SST. In this context, the latent heat E_q is approximated by a function that is proportional to the SST in the CP, serving as a bulk representation,

$$E_q = \alpha_q T_C. \quad (2.5)$$

As the SST increases, it is expected that convection and moisture will also increase, which modulates the atmosphere. The other two factors \bar{H} and \bar{Q} are also constants (Thual et al., 2014). A linear combination of \hat{K}_k , \hat{R}_k , \hat{Q}_k , and \hat{A}_k can also be utilized to reconstruct the wind and the MJO, where a temporal filter within the band 30 to 90 days is further carried out for reconstructing the MJO. Please refer to Appendix 6 for further details.

The skeleton model for the MJO (Majda and Stechmann, 2009) captures several key observational features: (i) the eastward propagation speed of 5 m/s, (ii) a dispersion rate of $d\omega/dk \approx 0$, and (iii) a horizontal quadrupole structure. The stochastic version (Thual et al., 2014) further simulates (iv) the intermittent generation of MJO events and (v) the organization of MJO events into wave trains that exhibit growth and dissipation. These properties are retained in the low-order representation provided in (2.3).

Unlike the box model used for the ENSO component in (2.1), the Fourier representation in (2.3) enables a more accurate depiction of the eastward propagation of the MJO's large-scale features. Since the modes $k = -1, -2$, and -3 are complex conjugates of those $k = 1, 2$, and

3, only 16 equations (four for each wavenumber, together with the mode $k = 0$) are needed for characterizing the intraseasonal atmospheric component.

The original stochastic skeleton model employed a stochastic birth-death process (Gardiner, 2009, Thual et al., 2014) to capture the irregularity of MJO events. It has been demonstrated that, in the limit of infinitesimal jumps, a continuous stochastic differential equation driven by white noise \dot{W}_A with a state-dependent coefficient can be derived (Chen and Majda, 2016). This formulation facilitates the spectral decomposition of the model and is the one utilized here. Although the system (2.3) is expressed in Fourier space, the state-dependent noises are easier to interpret when the system is presented in physical space. In physical space, the state-dependent noises in the equations for convective activity and moisture take the following form:

$$\sigma_A = \sqrt{\nu|Q|(A + \bar{A})}, \quad (2.6a)$$

$$\sigma_Q = \max(\tilde{\sigma}_Q(1 - e^{-c_q E_q}), \sigma_Q^{\min}), \quad (2.6b)$$

where ν , $\tilde{\sigma}_Q$, c_q , and σ_Q^{\min} are all positive constants. The noise coefficient σ_A in (2.6a), derived from the limit of infinitesimal jumps in the original stochastic skeleton model (Chen and Majda, 2016), indicates that the strength of the convective activity is dependent on the moisture level. This relationship is consistent with the deterministic part of the model, $\Gamma Q(A + \bar{A})$, where moisture influences the tendency of the SST temporal variation. On the other hand, the noise coefficient σ_Q links the ocean and the atmosphere via the latent heat variable E_q . Higher SST causes an increase in the latent heat, which strengthens the statistical coupling between the atmosphere and ocean. A minimum noise in the moisture process, denoted as σ_Q^{\min} , is prescribed to ensure that the noise coefficient remains non-negative. Since only the leading three Fourier modes are retained, the stochastic noises not only capture the explainable physics but also compensate for contributions from smaller scales.

The total wind τ appearing in (2.1) has two components:

$$\tau = u_W + \bar{u}_M, \quad (2.7)$$

where u_W represents the intraseasonal wind u reconstructed by K and R averaged over the western Pacific, the region where wind activity is most pronounced. The second component of the total wind is the interannual component, \bar{u}_M , which requires a separate governing equation.

2.4 Interannual wind

The interannual wind averaged over the western Pacific is driven by a simple process:

$$\frac{d\bar{u}_M}{dt} = -\lambda_M \bar{u}_M + \alpha_3 E_q + \sigma_M \dot{W}_M. \quad (2.8)$$

In this equation, the latent heat E_q from (2.5) acts as a forcing for the wind velocity. Together with the wind forcing in the interannual ocean model (2.1), this creates a feedback mechanism for air-sea interaction. The additional damping and stochastic terms introduce variability to the interannual wind that is not solely determined by latent heat. It is important to note that the fluctuations in interannual wind resulting from this noise are significantly weaker than those from the intraseasonal atmospheric model, allowing the latter to remain the dominant contributor to intraseasonal variability. See Figure 6.6 in Appendix 6. Nevertheless, the noise in (2.8) enhances the irregularity of the model simulation. It also establishes a more realistic dependence between latent heat and interannual wind, which prevents a purely deterministic relationship.

2.5 Spatiotemporal reconstruction

In the conceptual model developed here, ENSO is characterized by two SST indices, T_E and T_C , as described in (2.1). Similarly, the MJO is represented by the leading three Fourier modes in (2.3). Although both phenomena are represented in a low-dimensional form using time series, a spatiotemporal reconstruction based on these time series enables us to visualize the spatiotemporal patterns and spatial propagation of the observed features. The details and validation of the spatiotemporal reconstructions can be found in Appendix 6.

3 Datasets

Observational data is utilized to validate the simulated time series and statistics from the model.

3.1 ENSO data

The monthly SST data used in this study is sourced from the GODAS dataset (Behringer and Xue, 2004). The SST anomalies are calculated by subtracting the monthly mean climatology over the entire analysis period. The Niño 4 and Niño 3 indices represent the average SST anomalies over the zonal regions 160°E–150°W and 150°W–90°W, respectively, with a meridional average between 5°S and 5°N. The reanalysis period spans from 1982 to 2019, corresponding to the satellite era when observations are more reliable. This period is used to study ENSO-MJO spatiotemporal patterns. For statistical comparisons, a longer SST dataset (1950–2019) is used, obtained from the Extended Reconstructed Sea Surface Temperature version 5 (Huang et al., 2017).

The classification of different El Niño and La Niña events, which helps examine ENSO variability, is based on the criteria outlined in (Kug et al., 2009, Wang et al., 2019). These classifications rely on the average SST anomalies during boreal winter (December–January–February; DJF). An event is classified as an EP El Niño if the EP is warmer than the CP, and the EP SST anomaly exceeds 0.5°C. An extreme El Niño occurs when the maximum EP SST anomaly between April and the following March exceeds 2.5°C. A CP El Niño is identified when the CP is warmer than the EP, with a CP SST anomaly above 0.5°C. Lastly, a La Niña event is defined when the SST anomaly in either the CP or EP falls below −0.5°C.

3.2 MJO data

To represent convective activity (a), we use the National Oceanic and Atmospheric Administration’s (NOAA) interpolated outgoing longwave radiation (OLR) dataset (Liebmann and Smith, 1996). While several proxies for convective activity exist, OLR is chosen here as an initial, straightforward option for analysis. For other variables such as zonal wind, geopotential height, and specific humidity, we rely on the National Centers for Environmental Prediction–National Center for Atmospheric Research (NCEP–NCAR) reanalysis data (Kalnay et al., 1996). Both datasets offer a horizontal spatial resolution of $2.5^\circ \times 2.5^\circ$ and are available at daily temporal intervals. The period used for this study spans from 1982 to 2019 (Stechmann and Majda, 2015).

4 Results

4.1 ENSO statistics

Figure 4.1 presents the model simulations and associated statistics compared with observations. Panel (a) demonstrates that the simulated SST time series qualitatively match the observations. Notably, several large positive values are observed in T_E (e.g., at $t = 141$ and 145), corresponding to strong EP El Niño events. Similarly, there are periods (e.g., at $t = 129$ and 133) where both T_E and T_C exceed 0.5°C, with $T_C > T_E$, indicating CP events. Panels (b)–(d) compare key statistical measures. First, the model simulations exhibit power spectra very similar to the observations, reflecting the average oscillation period and its irregularity. Additionally, the model accurately reproduces the non-Gaussian probability density functions (PDFs), capturing the positive skewness and one-sided fat tail of the Niño 3 SST distribution. This allows the model to simulate extreme EP El Niño events and the El Niño–La Niña asymmetry. Likewise, the model captures the negative skewness of the Niño 4 SST distribution, preventing extreme events from occurring in the CP region. Furthermore, the model successfully reproduces the seasonal variation of SST variance, indicating a higher likelihood of event occurrence during boreal winter. Panel (e) shows the bivariate distribution of DJF SST peaks. Similar to observations, the strength of the SST peaks increases as events shift eastward in the Pacific, where CP events generally have weaker amplitudes than EP events in the model. Finally, Panel (f) displays the frequency of different ENSO events, which is a useful indicator of ENSO complexity. Overall, the model succeeds in reproducing the number of different ENSO events, consistent with nature. Appendix 6 contains the statistics of other variables, the role of the decadal variability I , and the reconstructed spatiotemporal fields. Particularly, the wind statistics also closely match the observations, capturing key features like positive skewness and a one-sided fat tail, which correspond to the westerly wind bursts, an important precursor for El Niño events.

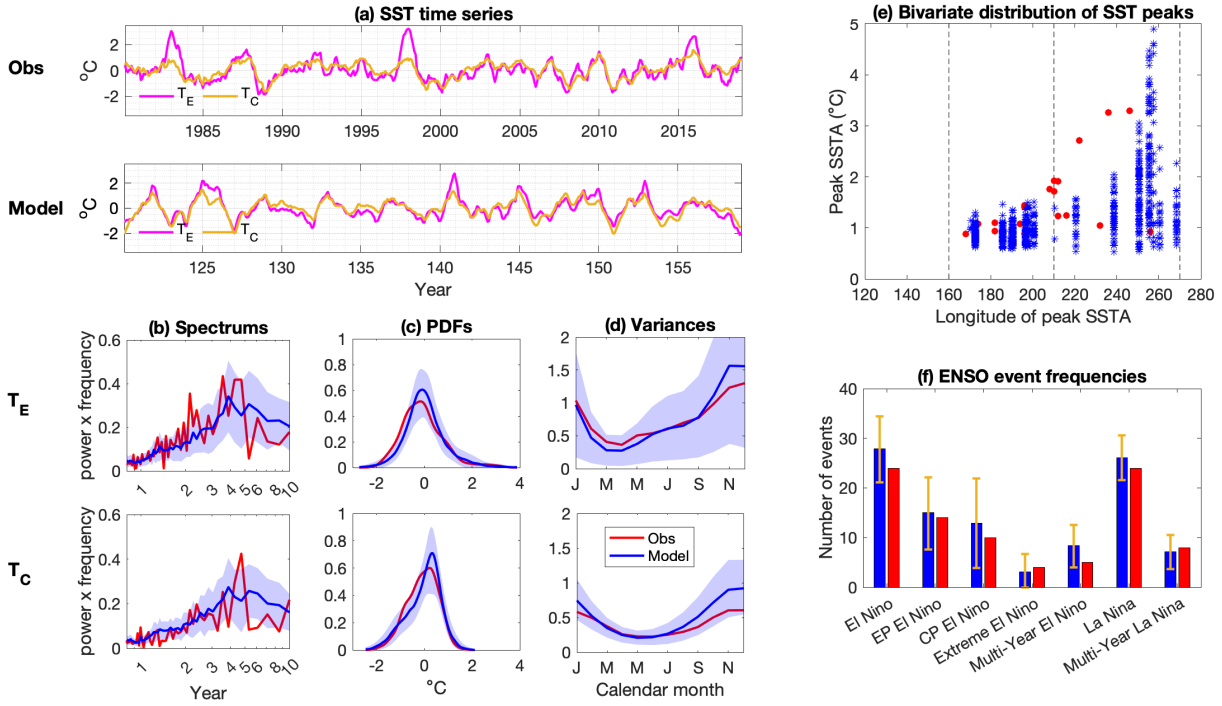


Figure 4.1: Comparison of model simulations and statistical data with observational records. Observations cover the period from 1950 to 2019 (a total of 70 years). The model simulation spans 2,000 years, with the first 40 years discarded as a burn-in period. The remaining simulations are divided into 28 non-overlapping segments, each corresponding to a 70-year observational period. Confidence intervals are calculated based on these 28 segments. Panel (a): Time series of T_E and T_C . Panels (b)–(d): Power spectra, PDFs, and variances as a function of months for T_E and T_C , with shaded areas representing 95% confidence intervals. Panel (e): Bivariate distribution of DJF SST peaks. Panel (f): Frequency of ENSO events over 70 years, with bars showing 95% confidence intervals. Model simulations are shown in blue, and observational data are shown in red.

4.2 MJO statistics

The atmospheric zonal velocity (u) and convective activity (A) are important variables for characterizing and reconstructing the MJO. The power spectra of these two variables are natural indicators to statistically describe the dominant spatiotemporal signal. The model simulation shows a high spectral density within the intraseasonal band (30 to 90 days) for modes $k = 1, 2$, and 3, indicating the dominant eastward-propagating MJO signal. Likewise, the westward-propagating moisture Rossby waves are captured by modes $k = -1, -2$, and -3 . The power spectra of the model within this intraseasonal band closely match observations. The results indicate that the model succeeds in capturing these crucial intraseasonal variabilities. See Figure 6.3 in the Appendix 6 for more details.

4.3 Spatiotemporal reconstructed field from the coupled model

Figure 4.2 shows the Hovmoller diagrams of the spatially reconstructed SST and MJO from the conceptual model. These diagrams illustrate the diversity and complexity of ENSO, as well as the coupled relationship between ENSO and the MJO. A similar figure based on observational data can be found in Appendix 6.

First, the model simulates different types of ENSO events with frequencies similar to observations (see also Panel (f) in Figure 4.1). A few examples of each type, with corresponding years of observed events in parentheses, are as follows: (i) moderate EP El Niño (1983): $t = 149$; (ii) extreme EP El Niño (1998): $t = 141$; (iii) delayed super El Niño (2014–2015): $t = 118$ –119; (iv) multi-year EP El Niño (1987–1988): $t = 123$ –126; (v) CP El Niño (2010): $t = 137$; (vi) multi-year CP El Niño (1993–1994): $t = 144$ –145; (vii) La Niña (2011): $t = 127$; (viii) multi-year La Niña (1999–2000): $t = 116$ –117. Additional examples can be found in Figure 6.5.

Second, the model successfully reproduces strong interactions between the MJO and ENSO.

Typically, intense MJO events are observed either preceding or during the El Niño phase, for both EP and CP El Niño events. The MJO signals extend further towards the EP, particularly during strong EP El Niño events. However, some MJO events are observed during La Niña phases (e.g., at $t=144$) or do not trigger ENSO events at all (e.g., at $t=131$). These findings are consistent with observations, as detailed in Appendix 6.

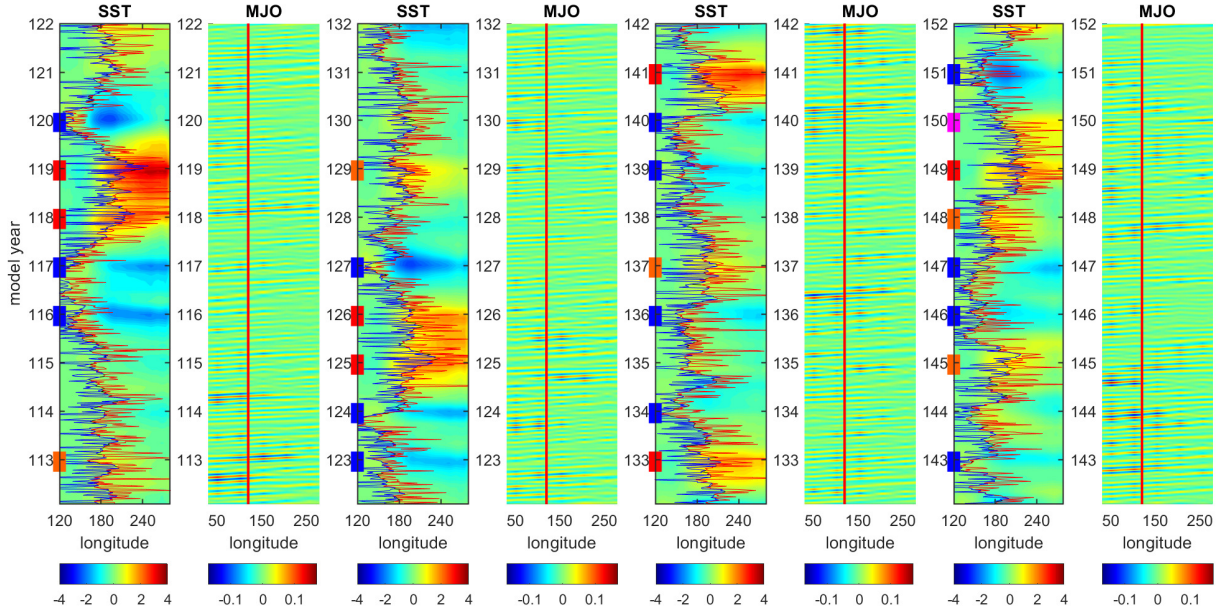


Figure 4.2: Hovmoller diagrams of the spatially reconstructed SST and MJO from the conceptual model. The x-axis of the SST Hovmoller diagram covers the equatorial Pacific, while the MJO diagram also includes the Indian Ocean. The red vertical line in the MJO panels marks the Western Pacific (WP) boundary at 120°E . In the SST panels, the averaged atmospheric wind over the WP is overlaid on the SST, with red and blue indicating westerly and easterly wind bursts, respectively. The black curve represents the interannual wind. The rectangles along the y-axis indicate different ENSO events occurring during boreal winter: strong and moderate EP El Niño (red), weak EP El Niño (purple), CP El Niño (orange), and La Niña (blue).

Figure 4.3 shows the lagged correlation between MJOI, an index representing the MJO averaged over the WP, or its strength $|\text{MJOI}|$, and an SST index, either T_C or T_E . This correlation is calculated specifically for years when El Niño events occur, aiming to highlight the statistical dependence between ENSO and the MJO. The analysis explores the lagged correlation across all El Niño events, including both EP and CP types (Panels (a)–(d)), as well as conditioning separately on EP events (Panels (e)–(f)) and CP events (Panels (g)–(h)).

Overall, the lagged correlations from the model simulations align well with observations. First, neither the simulations nor the observations provide clear evidence that MJOI statistically leads or lags SST (Thual et al., 2018), likely due to the faster oscillation and occurrence of the MJO on much shorter timescales. Consequently, the randomness of different MJO events tends to cancel out any consistent correlation with ENSO. However, the amplitude of the MJOI ($|\text{MJOI}|$) does show a correlation with SST, with the MJO becoming more intense prior to or during El Niño phases. Notably, the lagged correlation with T_E during all El Niño phases exhibits strong asymmetry, with a longer correlation observed before an El Niño event (Panel (a)). Such an extended correlation range reflects the process of MJO buildup and the triggering of El Niño events. After the El Niño peak, the MJO remains active for a few months until the SST anomaly dissipates. The model accurately captures this behavior, showing a similar lagged correlation pattern (Panel (b)). For T_C , the lagged correlation during all El Niño events resembles that with T_E in observations, though the model produces a slightly more symmetric correlation band. When conditioned only on CP events, the lagged correlation with T_C is more symmetric in both observations and model results (Panels (g)–(h)), with significant correlations

spanning a shorter window, from -5 to 5 months, compared to conditioning on all El Niño events. Finally, Panels (e)–(f) depict the lagged correlation with T_E conditioned on EP events. Although the model and observations have similar patterns, a stronger correlation is observed using the model outcomes. However, caution is needed when interpreting such a result since the number of EP events in the observational period is quite limited.

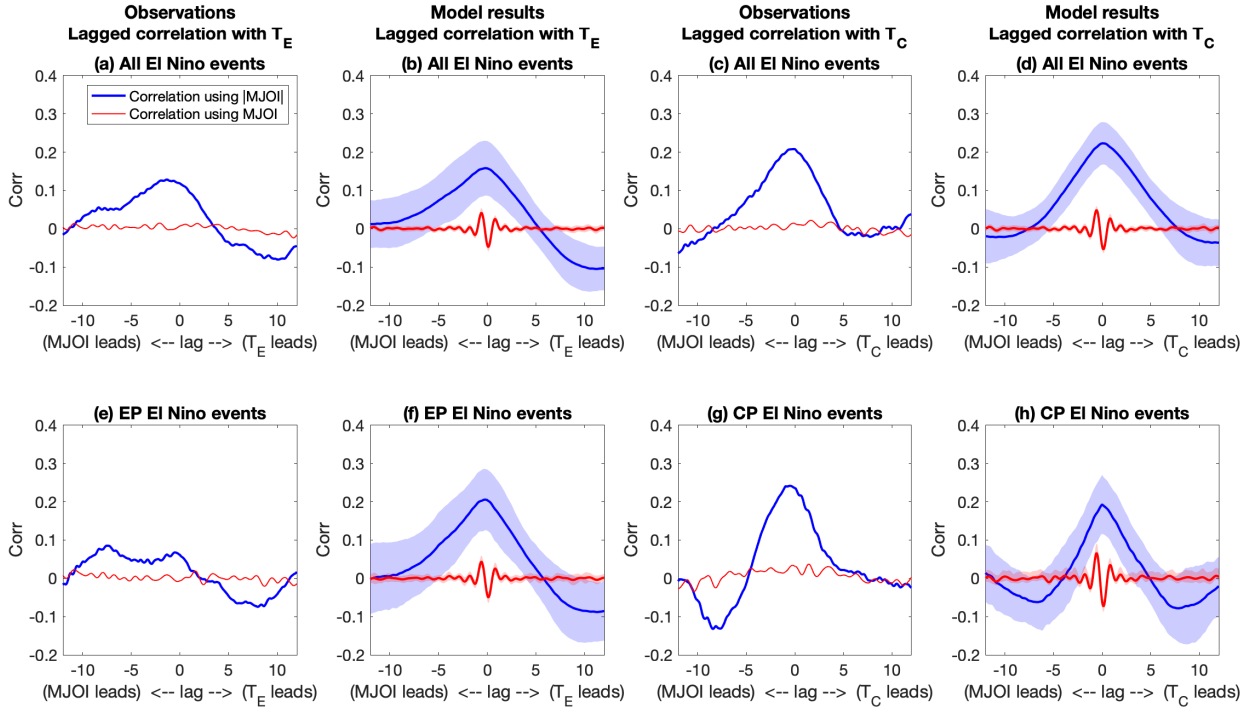


Figure 4.3: Lagged correlation between the MJO and ENSO. Panels (a)–(b): Lagged correlation with T_E for years when El Niño events occur. Panels (c)–(d): lagged correlation with T_C for the same years. Panels (e)–(f): Lagged correlation with T_E for years with only EP El Niño events. Panels (g)–(h): Lagged correlation with T_C for years with only CP El Niño events. On the x-axis, zero corresponds to the peak of the El Niño event, with the unit of the x-axis being months.

4.4 Role of state-dependent noises in the MJO equations

An important aspect to explore further is the role of the state-dependent noises, $\sigma_{\hat{Q}_k}(E_q)\dot{W}_{\hat{Q}_k}$ in (2.3c) and $\sigma_{\hat{A}_k}(Q, A)\dot{W}_{\hat{A}_k}$ in (2.3d). These noises are designed to capture statistical feedback from latent heat and generate intermittent MJO events, respectively. Without random noise in the moisture equation ($\sigma_{\hat{Q}_k} = 0$), the MJO is less affected by SST, resulting in fewer strong wind events and a weakened correlation between ENSO and MJO. Consequently, the model simulation will underestimate extreme El Niño occurrences and reduce non-Gaussian features. Conversely, when $\sigma_{\hat{A}_k} = 0$, MJO events become more regular, and the relationship between MJO and ENSO becomes more deterministic, resulting in a much larger correlation compared to observations. See Figures 6.7–6.9 in Appendix 6.

5 Conclusion

In this paper, we develop a stochastic conceptual model to describe the large-scale dynamics of the coupled ENSO and MJO systems. State-dependent noise is introduced alongside wind forcing and latent heat to enhance multi-scale statistical interactions, improving extreme event simulations. The model reproduces observed ENSO and MJO events and their statistical properties. Insights could guide improvements in complex models and reanalysis through multi-model data assimilation. Different theories exist for both ENSO and MJO dynamics. For example, MJO theories include the skeleton theory (used here) (Majda and Stechmann, 2009), moisture-mode theory (Adames and Kim, 2016), gravity-wave theory (Yang and Ingersoll, 2013), and trio-interaction theory (Wang et al., 2016). Similarly, there is debate on

whether ENSO variability is driven by a stable linear system forced by weather noise (Penland and Sardeshmukh, 1995, Moore and Kleeman, 1999), or it is intrinsically nonlinear (Jin et al., 2003, An and Jin, 2004). The conceptual model can potentially be adapted to test these theories to understand the roles of nonlinearity and noise in affecting ENSO dynamics.

6 Appendix: Supporting information

6.1 A brief overview of the stochastic skeleton model for the MJO

The MJO skeleton model is a nonlinear oscillator model for the MJO skeleton as a neutrally stable wave (Majda and Stechmann, 2009, 2011). The core mechanism behind this oscillation is the interaction between (i) planetary-scale lower-tropospheric moisture anomalies, denoted by q , and (ii) subplanetary-scale convection and wave activity, represented by a . The planetary envelope, $a \geq 0$, characterizes the collective influence of unresolved subplanetary convection and wave activity. A critical aspect of the q - a interaction lies in the assumption that moisture anomalies q directly affect the rate of change of a , expressed by the relation $a_t = \Gamma qa$, where $\Gamma > 0$ is a constant governing the strength of this interaction.

In the skeleton model, the interaction between moisture anomalies (q) and convection/wave activity (a) is further coupled with the linearized primitive equations projected onto the first vertical baroclinic mode. The non-dimensionalized system of equations is given as follows:

$$u_t - yv - \theta_x = 0, \quad (6.1a)$$

$$yu - \theta_y = 0, \quad (6.1b)$$

$$\theta_t - u_x - v_y = \bar{H}a - s^\theta, \quad (6.1c)$$

$$q_t + \bar{Q}(u_x + v_y) = -\bar{H}a + s^q, \quad (6.1d)$$

$$a_t = \Gamma qa, \quad (6.1e)$$

with periodic boundary conditions along the equatorial belt and planetary-scale equatorial long-wave scaling. In the dry dynamics ((6.1a)–(6.1c)), u , v , and θ represent zonal velocity, meridional velocity, and potential temperature, respectively, while (6.1d) governs the evolution of low-level moisture (q). All variables are anomalies from a radiative-convective equilibrium, except for a . The skeleton model incorporates a minimal set of parameters: \bar{Q} represents the background vertical moisture gradient, and Γ is a proportionality constant for the q - a interaction. While \bar{H} is not dynamically influential, it defines a cooling/drying rate $\bar{H}a$ in dimensional terms. External cooling and moistening effects, s^θ and s^q , must be prescribed to complete the system.

Next, the system (6.1) is projected onto the first Hermite function in the meridional direction, where the fields are represented as $a(x, y, t) = \tilde{A}(x, t)\phi_0$, $q = Q\phi_0$, $s^q = S^q\phi_0$, $s^\theta = S^\theta\phi_0$, where $\phi_0(y) = \sqrt{2}(4\pi)^{-1/4}\exp(-y^2/2)$. This choice of meridional heating structure excites only Kelvin waves and the first symmetric equatorial Rossby waves. The resulting meridionally truncated system is:

$$K_t + K_x = (S^\theta - \bar{H}\tilde{A})/2, \quad (6.2a)$$

$$R_t - R_x/3 = (S^\theta - \bar{H}\tilde{A})/3, \quad (6.2b)$$

$$Q_t + \bar{Q}(K_x - R_x/3) = (\bar{H}\tilde{A} - S^q)(\bar{Q}/6 - 1), \quad (6.2c)$$

$$\tilde{A}_t = \Gamma Q\tilde{A}, \quad (6.2d)$$

provided that $S^\theta = S^q$. Note that \tilde{A} represents the total convective activity, namely the summation of the anomaly A and the background state \bar{A} . The dry dynamics components can be reconstructed as follows:

$$\begin{aligned} u &= (K - R)\phi_0 + R\phi_2/\sqrt{2}, \\ v &= (4\partial_x R - \bar{H}\tilde{A})\phi_1/3\sqrt{2}, \\ \theta &= -(K + R)\phi_0 - R\phi_2/\sqrt{2}. \end{aligned} \quad (6.3)$$

Here, the higher-order Hermite functions $\phi_1(y) = 2y(4\pi)^{-1/4}\exp(-y^2/2)$ and $\phi_2(y) = (2y^2 - 1)(4\pi)^{-1/4}\exp(-y^2/2)$, though irrelevant to the dynamics, are necessary for retrieving the MJO's quadruple structure (Majda and Stechmann, 2009).

The original stochastic skeleton model (Thual et al., 2014) introduces a simple stochastic parameterization to represent synoptic-scale processes. In this model, the amplitude equation (6.1e) or (6.2d) is replaced by a stochastic birth-death process, which allows for intermittent fluctuations in the synoptic activity envelope (Gardiner, 2009). Let \tilde{A} be a random variable taking discrete values $\tilde{A} = \Delta\tilde{A}\eta$, where η is a positive integer. The transition probabilities between states over a time step Δt are given by:

$$\begin{aligned} P\{\eta(t + \Delta t) = \eta(t) + 1\} &= \lambda\Delta t + o(\Delta t), \\ P\{\eta(t + \Delta t) = \eta(t) - 1\} &= \mu\Delta t + o(\Delta t), \\ P\{\eta(t + \Delta t) = \eta(t)\} &= 1 - (\lambda + \mu)\Delta t + o(\Delta t), \\ P\{\eta(t + \Delta t) \neq \eta(t) + 1, \eta(t), \eta(t) + 1\} &= o(\Delta t), \end{aligned} \quad (6.4)$$

where λ and μ are the birth and death rates defined as:

$$\lambda = \begin{cases} \Gamma|q|\eta + \delta_{\eta 0} & \text{if } q \geq 0 \\ \delta_{\eta 0} & \text{if } q < 0 \end{cases} \quad \text{and} \quad \mu = \begin{cases} 0 & \text{if } q \geq 0 \\ \Gamma|q|\eta & \text{if } q < 0 \end{cases} \quad (6.5)$$

with $\delta_{\eta 0}$ being the Kronecker delta operator. These transition rates ensure that $\partial_t E(\tilde{A}) = \Gamma E(Q\tilde{A})$ for $\Delta\tilde{A}$ small, recovering the average $Q\tilde{A}$ interaction described (6.1).

In (Chen and Majda, 2016), a continuous stochastic differential equation (SDE) for convective activity is derived for small Δa :

$$\frac{d\tilde{A}}{dt} = \Gamma Q\tilde{A} + \sqrt{\Delta\tilde{A}\Gamma|Q|\tilde{A}}\dot{W}_A. \quad (6.6)$$

where \dot{W}_A represents a standard Wiener process, capturing the stochastic fluctuations in convective activity.

The leading three Fourier modes from the system (6.2a)–(6.2c), along with the stochastic equation (6.6), are employed to construct a conceptual model for the atmospheric intraseasonal component. It aims to capture the essential large-scale dynamics and provide a simplified yet effective representation of intraseasonal atmospheric processes.

6.2 Reconstruction of the MJO from the characteristic variables

The structure of the MJO can be characterized by the eigenvector associated with the linearized form of (6.2). Let $\mathbf{U} = (K, R, Q, A)^T$ represent the collection of state variables in (6.2). By assuming a plane-wave ansatz for \mathbf{U} and substituting it into (6.2), we derive an eigenvalue problem for each wavenumber k . This results in a four-dimensional system that features four eigenmodes: dry Kelvin, moisture Kelvin, dry Rossby, and MJO. Each of these waves can be expressed as a linear combination of K, R, Q and A .

Let the eigenvalue corresponding to the MJO for wavenumber k be denoted as follows:

$$\omega_k := \omega_{\text{MJO}}(k).$$

The evolution of the MJO for wavenumber k is then represented by the time series of the Fourier coefficients $\hat{K}_k, \hat{R}_k, \hat{Q}_k$, and \hat{A}_k projected onto the eigenvector associated with ω_k . The numerical values of the eigenvalues and eigenvectors pertaining to the MJO modes are presented in Table 1.

k	$\omega_{\text{MJO}}(k)$	\hat{K}	\hat{R}	\hat{Q}	\hat{A}
1	0.0261	0.4577 <i>i</i>	-0.4088 <i>i</i>	-0.2513 <i>i</i>	0.7485
2	0.0304	0.2343 <i>i</i>	-0.2857 <i>i</i>	-0.3389 <i>i</i>	0.8652
3	0.0309	0.1537 <i>i</i>	-0.2177 <i>i</i>	-0.3561 <i>i</i>	0.8956

Table 1: Eigenvalues $\omega_{\text{MJO}}(k)$ and eigenvectors $\hat{\mathbf{e}}_{\text{MJO}}(k)$ for the MJO skeleton are shown for zonal wavenumbers $k = 1, 2$, and 3 . The frequencies are presented in units of cycles per day (cpd). The model parameters are listed in Table 2.

It is worth noting that the frequencies of the first three modes remain nearly constant. The final step in constructing the MJO signal involves summing the modes for $k = 1, 2$, and $k = 3$, followed by the application of a temporal filter to retain only the signals within the intraseasonal band, specifically between 30 and 90 days.

6.3 Processing the observational data for the intraseasonal atmospheric model

The processing of observational data for the intraseasonal atmospheric model follows the procedure outlined in (Stechmann and Majda, 2015).

Zonal velocity u : The zonal velocity data set contains values at different layers in the vertical direction. The MJO skeleton model takes into account only the first baroclinic mode of u , which is defined by the following expression:

$$u := u_{BC,1} = \frac{u(850\text{hPa}) - u(200\text{hPa})}{2\sqrt{2}}. \quad (6.7)$$

Geopotential temperature θ : The geopotential temperature dataset, denoted as θ , is related to the geopotential height Z , which is also measured at various vertical layers. The first baroclinic mode of θ is expressed as follows:

$$\theta := \theta_{BC,1} = -Z_{BC,1} = -\frac{Z(850\text{hPa}) - Z(200\text{hPa})}{2\sqrt{2}}. \quad (6.8)$$

The reference scales θ and Z are approximately $\bar{\alpha} \approx 15.6$ K and $c^2/g \approx 265$ m, respectively. To achieve non-dimensionalization, the geopotential height data Z is divided by c^2/g for non-dimensionalization.

Moisture Q : The variable Q represents the lower tropospheric anomaly of water vapor near 850 hPa and is defined as follows:

$$Q = \frac{1}{4}q(925\text{hPa}) + \frac{1}{2}q(850\text{hPa}) + \frac{1}{4}q(725\text{hPa}). \quad (6.9)$$

Note that in the datasets for q , data at the 725 hPa level is unavailable; therefore, the data from the 700 hPa level is used instead. Additionally, Q has been non-dimensionalized using the natural reference scale $L_v/c_p\tilde{\alpha}$, where $\tilde{\alpha}$ represents the reference potential temperature scale.

Convective activity A : The outgoing longwave radiation (OLR) is used as a surrogate for A and is expressed by the following relationship:

$$\bar{H}A = -H_{\text{OLR}} \times \text{OLR}, \quad (6.10)$$

where $H_{\text{OLR}} = 0.06\text{Kday}^{-1} (\text{Wm}^{-2})^{-1}$ is an estimated constant.

Using the meridional basis functions, the definitions of the Kelvin wave K and the first symmetric equatorial Rossby wave R are given by:

$$\begin{aligned} K &= \frac{1}{2}(u_0 - \theta_0) \text{ and} \\ R &= -\frac{1}{4}(u_0 + \theta_0) + \frac{\sqrt{2}}{4}(u_2 - \theta_2), \end{aligned} \quad (6.11)$$

where u_m and θ_m represent the meridional projections.

6.4 Model parameters

The values and definitions of the constant parameters in the conceptual model are listed in Table 2. In addition to these, the model uses functions of time and state variables for some parameters. The wind coefficients,

$$\beta_E(I) = \frac{\sqrt{0.6} \left(8 - \frac{4I}{5}\right)}{3}, \quad (6.12a)$$

$$\beta_C(I) = 0.8\beta_E(I), \quad (6.12b)$$

$$\beta_u(I) = -0.4\beta_E(I), \quad (6.12c)$$

$$\beta_h(I) = -0.2\beta_E(I), \quad (6.12d)$$

which appear in (2.1), are some of the variable parameters in the model. Such functions incorporate the decreased sensitivity to changes in wind during periods of strong Walker circulation.

Other parameters that are non-constant include the damping coefficients $c_1(T_C, t)$ and $c_2(t)$ in (2.1). Both are sinusoidal functions of time in order to reproduce the observed seasonal phase locking of SST in the CP and EP. In addition, c_1 is a quadratic function of T_C which allows

the model to produce the negatively skewed PDF for CP SST anomalies. Specifically, they are expressed as

$$c_1(T_C, t) = 0.78 \left[25(T_C + 0.1)^2 + 0.6 \right] \left[1 + 0.6 \sin \left(\frac{2\pi}{6} t \right) \right], \quad (6.13a)$$

$$c_2(t) = 0.84 \left[1 + 0.4 \sin \left(\frac{2\pi}{6} t + \frac{2\pi}{6} \right) + 0.4 \sin \left(\frac{4\pi}{6} t + \frac{2\pi}{6} \right) \right]. \quad (6.13b)$$

The state dependent noise coefficient $\sigma_I(I)$ in (2.2) can be derived using the Fokker-Planck equation evaluated at the stationary solution of the PDF for I, $p(I)$ (Averina and Artemiev, 1988). The resulting noise coefficient is

$$\sigma_I(I) = Re \left(\sqrt{-8\lambda \int_0^I \lambda(y - \bar{I}) dy} \right). \quad (6.14)$$

Parameter	Definition	Value
r	Collective ocean adjustment rate	0.15
α_1	Scaling factor to reflect the thermocline feedback on T_C	0.0225
α_2	Scaling factor to reflect the thermocline feedback on T_E	0.075
b_0	Upper bound estimation of the thermocline tilt	2.5
μ	Relative coupling coefficient	0.5
γ	Thermocline feedback strength	0.45
ρ	Coupling coefficient for zonal advection and decadal variability	0.12
C_U	Correction term to ensure non-linear T_C has a mean of 0	0.009
λ	Decadal variable damping rate	0.0333
\bar{I}	Decadal variable mean state	2
d_k	Atmospheric damping rate	4.2
\bar{H}	Heating/drying rate	38.8235
\bar{Q}	Background vertical moisture gradient	0.9
Γ	Constant of proportionality	292.9412
λ_A	Convective activity damping rate	2
ν	Convective noise scaling factor	0.25
$\tilde{\sigma}_Q$	Maximum moisture noise amplitude	2
c_q	Latent heat sensitivity	0.5
σ_Q^{min}	Minimum moisture noise amplitude	0.0067
α_q	Latent heat sensitivity to SSTA in the CP	0.9
λ_M	Interannual wind damping rate	0.3333
α_3	Interannual wind sensitivity to latent heat	0.03
σ_M	Interannual wind noise amplitude	0.024

Table 2: Definitions and values for the constant parameters in the coupled model.

The model uses non-dimensional variables. The dimensional units of each variable are listed in Table 3.

Variable	Units	Variable	Units	Variable	Units
$[U]$	1.5 m/s	$[h_W]$	150 m	$[T]$	7.5 °C
$[\tau]$	50 m/s	$[Q]$	15 K	$[A]$	151 K ⁻¹
$[\theta]$	15 K	$[t]$	2 months	$[x]$	15000 km

Table 3: Dimensional units of the model variables.

6.5 Reconstruction of the ENSO spatiotemporal patterns using bivariate regression

Recall that the stochastic conceptual model includes two SST variables, T_C and T_E , as defined in (2.1). These variables can be used to approximately reconstruct the entire SST field across the equatorial Pacific. The method employed here is a bivariate regression,

$$\text{SST}(x, t) = a_E(x)T_E(t) + a_C(x)T_C(t), \quad (6.15)$$

where $a_E(x)$ and $a_C(x)$ are the spatial basis functions that depends on the location x .

For each longitude x^* , the two scalar regression coefficients, $a_E(x^*)$ and $a_C(x^*)$, are computed using (6.15) based on observational SST anomaly data from 1980 to 2020. Repeating this process across all longitude grids yields the spatially dependent functions $a_E(x)$ and $a_C(x)$. These functions are displayed in Panel (a) of Figure 6.1. The regression coefficient function $a_C(x)$ ($a_E(x)$) peaks in the CP (EP) region, as the SST at those longitudes is closely correlated with T_C (T_E).

Given that the spatiotemporal reconstruction based on this bivariate regression is applied to study the coupled ENSO-MJO phenomena, it is crucial to validate the accuracy of the reconstructed field. Panels (b) and (c) of Figure 6.1 compare the actual SST field with the reconstructed one, while Panel (d) presents their difference. Overall, the reconstructed field almost perfectly captures the exact SST patterns, especially in the EP and CP regions, with only minor biases in the WP and along the eastern boundary.

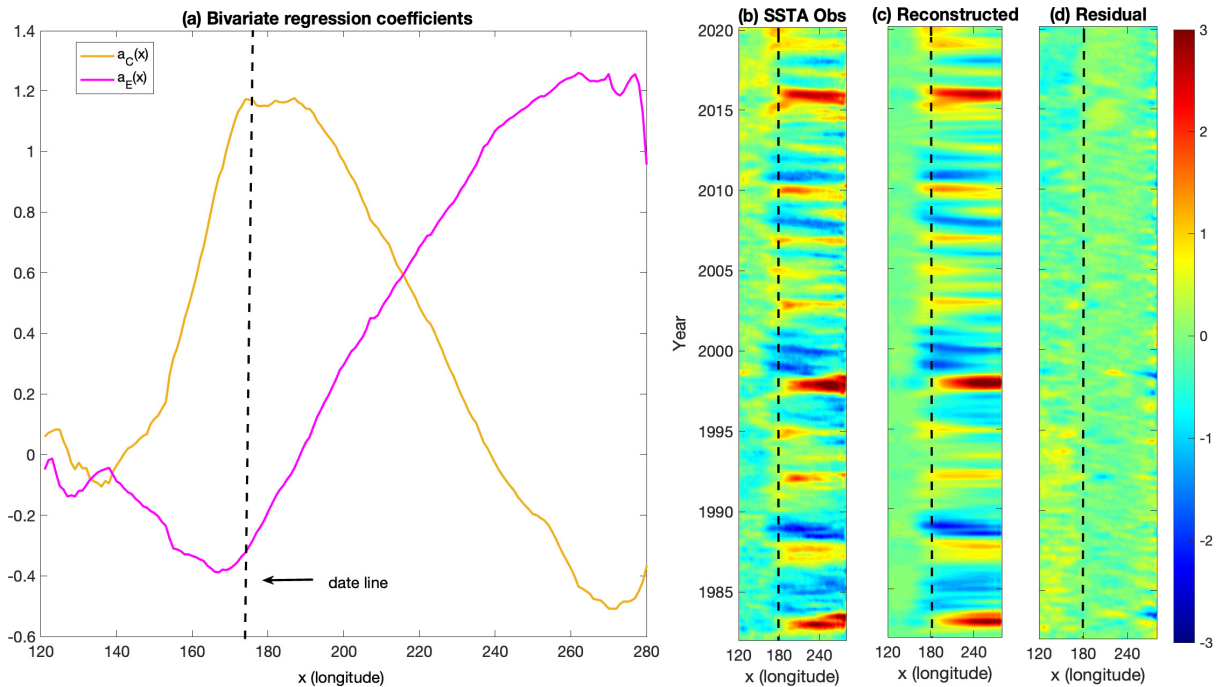


Figure 6.1: Bivariate regression analysis. Panel (a): Regression coefficients $a_E(x)$ and $a_C(x)$ from (6.15). Panel (b): Observed sea surface temperature (SST) field. Panel (c): Reconstructed SST field based on the bivariate regression using the coefficients from Panel (a). Panel (d): Residual SST, representing the difference between the observed SST in Panel (b) and the reconstructed SST in Panel (c).

6.6 Reconstruction of the MJO spatiotemporal patterns using Fourier summation

The reconstruction of the intraseasonal atmospheric variables, which can further describe the spatiotemporal patterns of the MJO, is given by the Fourier summation. For instance, the reconstruction of the moisture variable Q in (2.3) in physical space is expressed as:

$$Q(x, t) = \sum_{k=\pm 1, \pm 2, \pm 3} \hat{Q}(t)e^{ikx}. \quad (6.16)$$

6.7 The ENSO-MJO spatiotemporal patterns in observational data

Figure 6.2 presents Hovmoller diagrams of ENSO and MJO patterns during the observational period from 1982 to 2018. Similar to Figure 4.2, the SST spans the equatorial Pacific, while the MJO also extends into the Indian Ocean. The red vertical line in the MJO panels marks the boundary of the Western Pacific (WP) at 120°E. In the SST panels, the averaged atmospheric wind over the WP is overlaid on the SST, with red and blue indicating westerly and easterly wind bursts, respectively. The black curve represents the interannual wind. This figure is used to qualitatively validate the coupled relationship between ENSO and MJO as illustrated in the stochastic conceptual model shown in Figure 4.2.

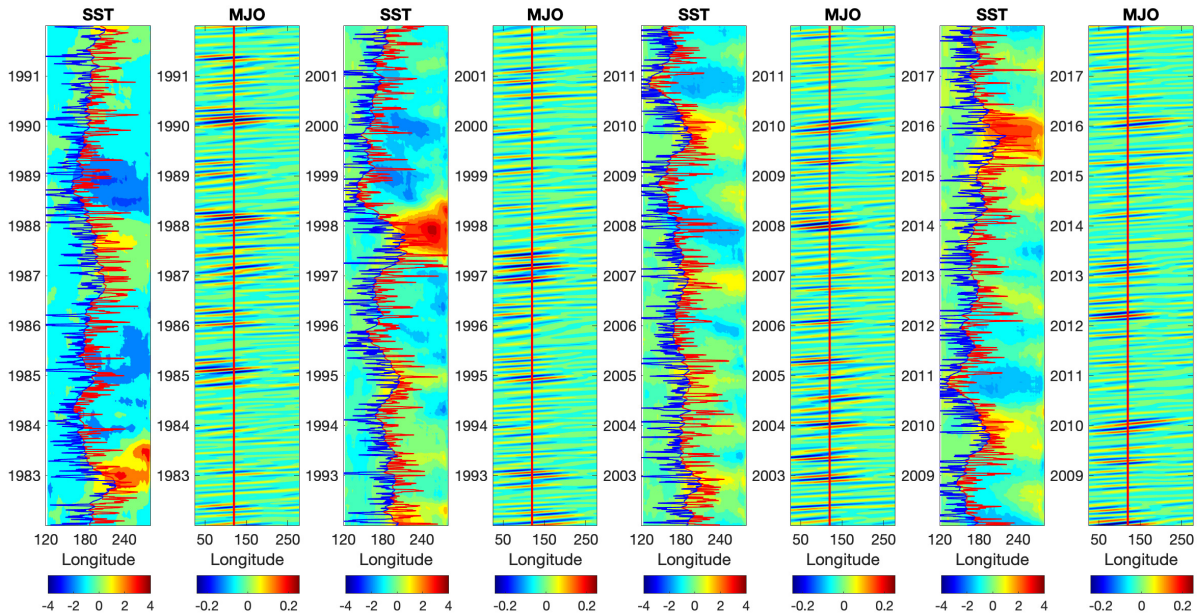


Figure 6.2: Hovmoller diagrams depicting the evolution of ENSO and MJO patterns during the observation period from 1982 to 2018. The format is similar to Figure 4.2.

6.8 MJO statistics

Figure 6.3 presents the power spectra of atmospheric zonal velocity (u) and convective activity (A), two key variables for reconstructing the MJO. The x-axis spans wavenumbers from $k = -3$ to $k = 3$, which are the wavenumbers used in the model. The y-axis represents frequency in cycles per day (cpd). The focus is on the intraseasonal band, highlighted between the two horizontal dashed lines. Black dots mark the dispersion curves from linear analysis of the MJO skeleton model. The high density within this band for modes $k = 1, 2$, and 3 indicates the dominant eastward-propagating MJO signal. Conversely, the westward-propagating moisture Rossby waves are captured by modes $k = -1, -2$, and -3 . The power spectra of the model within the intraseasonal band resemble observations. On the other hand, the model underestimates the power density at lower frequencies (where cpd approaches zero). This is because the observations contain information across all temporal scales, whereas this model is primarily designed to capture intraseasonal variabilities. Further, the model density patterns at higher frequencies for modes $k = 1, 2$, and 3 are pretty consistent with observations. The modes with negative wavenumbers in the model have stronger spectral density, possibly due to the stochastic noise. Since the model only focuses on coupling MJO and ENSO, matching the higher frequency signals does not impact the model's function. Note that the primary mechanism through which SST drives the intraseasonal model is the state-dependent noise coefficient on moisture, representing statistical feedback that does not directly affect the mean state of intraseasonal variability.

Figure 6.4 presents the standard deviation of MJO as a function of longitude conditioned on CP and EP El Niño events. The longitudes span from the prime meridian to 70°W. The

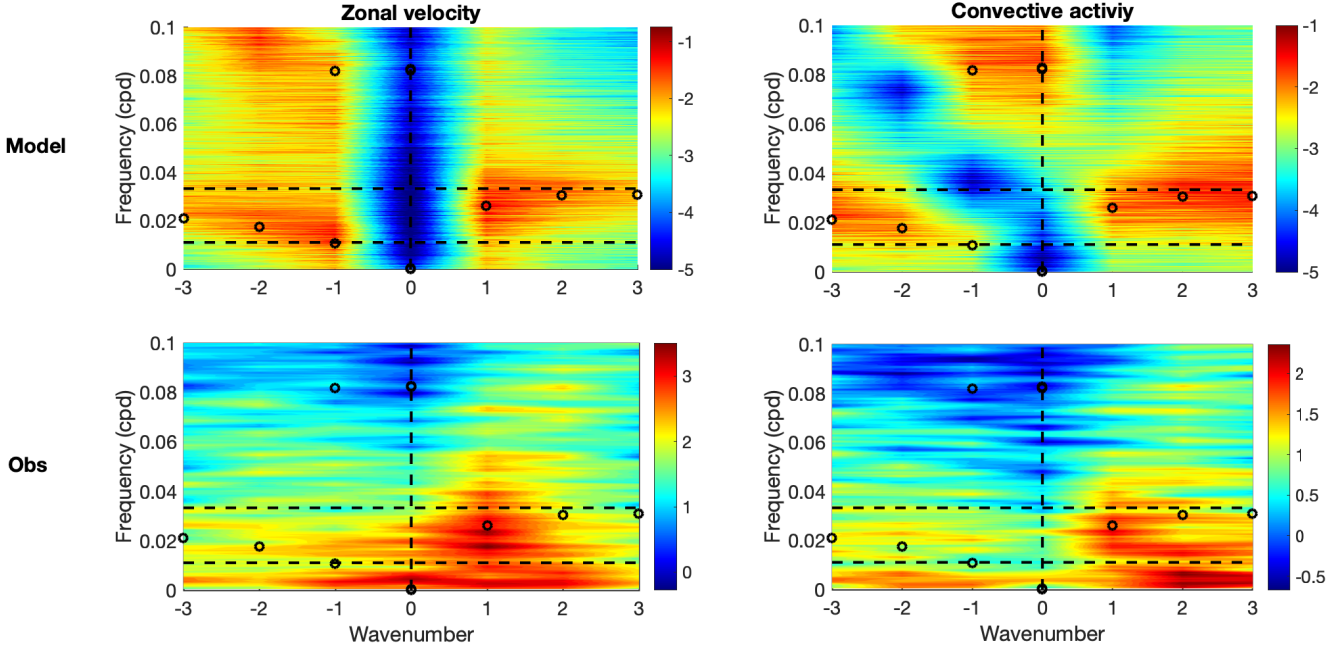


Figure 6.3: Power spectra of atmospheric zonal velocity (u) and convective activity (A). The x-axis represents wavenumbers, while the y-axis shows frequency in cycles per day (cpd). As the conceptual model includes only the first three Fourier modes, the x-axis is limited to modes $k = \pm 3$. The top panels display results from the coupled model, and the bottom panels show observations. Black dots indicate the dispersion curves from linear analysis of the MJO skeleton model. The two dashed horizontal lines represent the intraseasonal band, spanning from 30 days (0.333 cpd) to 90 days (0.111 cpd).

warm pool region, which includes the Indian Ocean and the WP, is highlighted by dashed lines. The high MJO activity in this region indicates that the warm SSTs fuel the MJO. Additionally, the standard deviation of MJO during EP El Niño events is higher than that of CP El Niño events in the eastern Pacific while the opposite is true in the warm pool region for both the model simulation and observations. Note that the amplitude of the MJO signal in the model is slightly weaker than that of observations since the model is coarse grained and thus averages the high frequency larger amplitudes.

6.9 Additional analysis of the coupled ENSO-MJO model

Figure 6.5 presents additional model results. While the main text focuses on the two SST variables, this figure includes time series and statistics for other variables in the stochastic conceptual model. The thermocline in the WP, h_W , exhibits statistics comparable to observations. The wind statistics closely match the observations, capturing key features like positive skewness and a one-sided fat tail, which correspond to the westerly wind bursts, an important precursor for El Niño events. Accompanying the time series, Hovmoller diagrams of SST and MJO during the same period are also shown. Notably, the decadal variability I is more pronounced after $t = 510$, resulting in a stronger zonal ocean advection effect (see (2.1c)). Consequently, more CP El Niño events are observed during this period compared to the prior half of the simulation. In contrast, when I approaches zero before $t = 510$, several strong EP El Niño events occur, along with more active MJO events.

Figure 6.6 displays T_E alongside the two wind components in the WP: the interannual wind (u_W) and the intraseasonal wind (\bar{u}_M). The interannual wind is closely synchronized with T_E , showing only minor fluctuations due to randomness. However, the amplitude of this randomness is much smaller than that of the intraseasonal wind, which is linked to the MJO. As a result, variability in the interannual wind does not significantly overshadow the signals from the intraseasonal model.

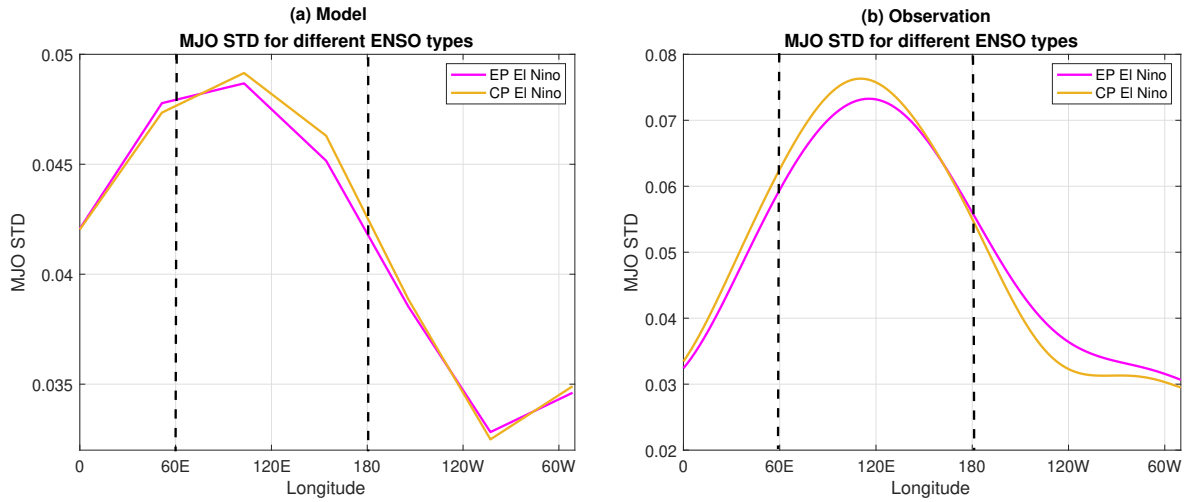


Figure 6.4: Standard deviation of MJO plotted as a function of longitude during EP El Niño events (purple) and CP El Niño events (orange). (a) displays the zonal standard deviation produced by the model and (b) the shows the zonal standard deviation from observation. The dashed black lines mark the western boundary of the Indian Ocean and the eastern boundary of the WP.

Figure 6.7 compares three model configurations: the full model (Panel (a)), the model without state-dependent noise in the convective activity ($\sigma_{\hat{A}_k} = 0$ in (2.3d); Panel (b)), and the model without state-dependent noise in the moisture process ($\sigma_{\hat{Q}_k} = 0$ in (2.3c); Panel (c)). When state-dependent noise is removed from the convective activity process (2.3d) (Panel (b)), the intermittent behavior of the MJO vanishes, and the occurrences of MJO and ENSO become more synchronized, diverging from natural behavior. This also introduces a significant bias in the lagged regression between MJO and ENSO, as seen in Figure (6.8). In contrast, when state-dependent noise is removed from the moisture process (2.3c) (Panel (c)), the intermittency is restored. However, in the absence of SST feedback, which is an external driving force for the MJO, strong MJO events are severely underestimated. Consequently, extreme El Niño events are harder to trigger, resulting in biases in reproducing the non-Gaussian, fat-tailed statistics of ENSO. Additionally, the lack of SST feedback drastically weakens the correlation between SST and the MJO as seen in Figure 6.9.

Figure 6.8 presents the lagged correlation between MJO and ENSO when the state-dependent noise in convective activity is removed ($\sigma_{\hat{A}_k} = 0$), based on the MJOI and SST time series. Compared with the full model results, as shown in Figure 4.3, the lagged correlation without this noise is significantly higher than observed. As a result, the relationship between MJO and ENSO becomes much more deterministic, deviating from the natural system. The findings here highlight the crucial role of state-dependent noise in convective activity, which is essential for generating the many intermittent MJO events seen in nature.

Similarly, figure 6.9 depicts the lagged correlation between MJOI and SST time series for the model with no noise in the low-level moisture equation. In comparison with observations, and the full model results (Figure 4.3), without this noise the link between MJO and SST is severely weakened. Removing this state dependent noise breaks the feedback loop between the atmospheric and oceanic components. Ultimately wind bursts are significantly reduced thus inhibiting the formation of extreme El Niño events and in turn reducing MJO activity.

Open Research

The code used to process the data and create the figures was written in MATLAB. The code and output data of the experiments are available on Github:

https://github.com/charrosemoser/ENSO_MJO_Stochastic_Conceptual_Model.

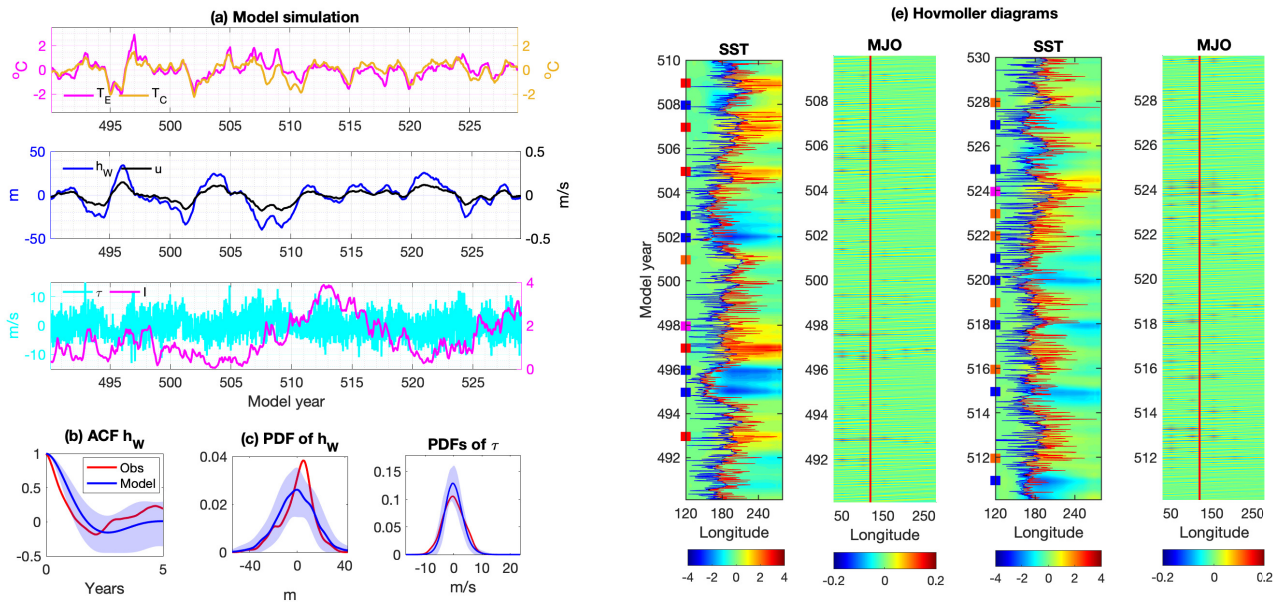


Figure 6.5: Additional model simulation results. Panel (a): Time series of model variables: sea surface temperatures in the eastern and central Pacific (T_E and T_C), thermocline depth in the western Pacific (h_W), ocean zonal current in the central Pacific (u), total wind in the western Pacific (τ), and decadal variability (I). Panels (b)-(c): ACF and PDF of h_W , comparing model results with observations. Panel (d): PDF of τ . Panel (e): Hovmöller diagram of SST and MJO over the same period shown in Panel (a).

Acknowledgments

The research of N.C. is funded by Office of Naval Research N00014-24-1-2244. C.M. and Y.Z. are partially supported as research assistants under this grant.

References

- Chester F Ropelewski and Michael S Halpert. Global and regional scale precipitation patterns associated with the El Niño/Southern Oscillation. *Monthly Weather Review*, 115(8):1606–1626, 1987.
- Michael J McPhaden, Stephen E Zebiak, and Michael H Glantz. ENSO as an integrating concept in earth science. *Science*, 314(5806):1740–1745, 2006a.
- Mojib Latif, D Anderson, T Barnett, M Cane, R Kleeman, A Leetmaa, J O’Brien, A Rosati, and E Schneider. A review of the predictability and prediction of enso. *Journal of Geophysical Research: Oceans*, 103(C7):14375–14393, 1998.
- J David Neelin, David S Battisti, Anthony C Hirst, Fei-Fei Jin, Yoshinobu Wakata, Toshio Yamagata, and Stephen E Zebiak. ENSO theory. *Journal of Geophysical Research: Oceans*, 103(C7):14261–14290, 1998.
- Antonietta Capotondi, Andrew T Wittenberg, Matthew Newman, Emanuele Di Lorenzo, Jin-Yi Yu, Pascale Braconnot, Julia Cole, Boris Dewitte, Benjamin Giese, Eric Guilyardi, et al. Understanding ENSO diversity. *Bulletin of the American Meteorological Society*, 96(6):921–938, 2015.
- Axel Timmermann, Soon-Il An, Jong-Seong Kug, Fei-Fei Jin, Wenju Cai, Antonietta Capotondi, Kim M Cobb, Matthieu Lengaigne, Michael J McPhaden, Malte F Stuecker, et al. El Niño–Southern Oscillation complexity. *Nature*, 559(7715):535–545, 2018.

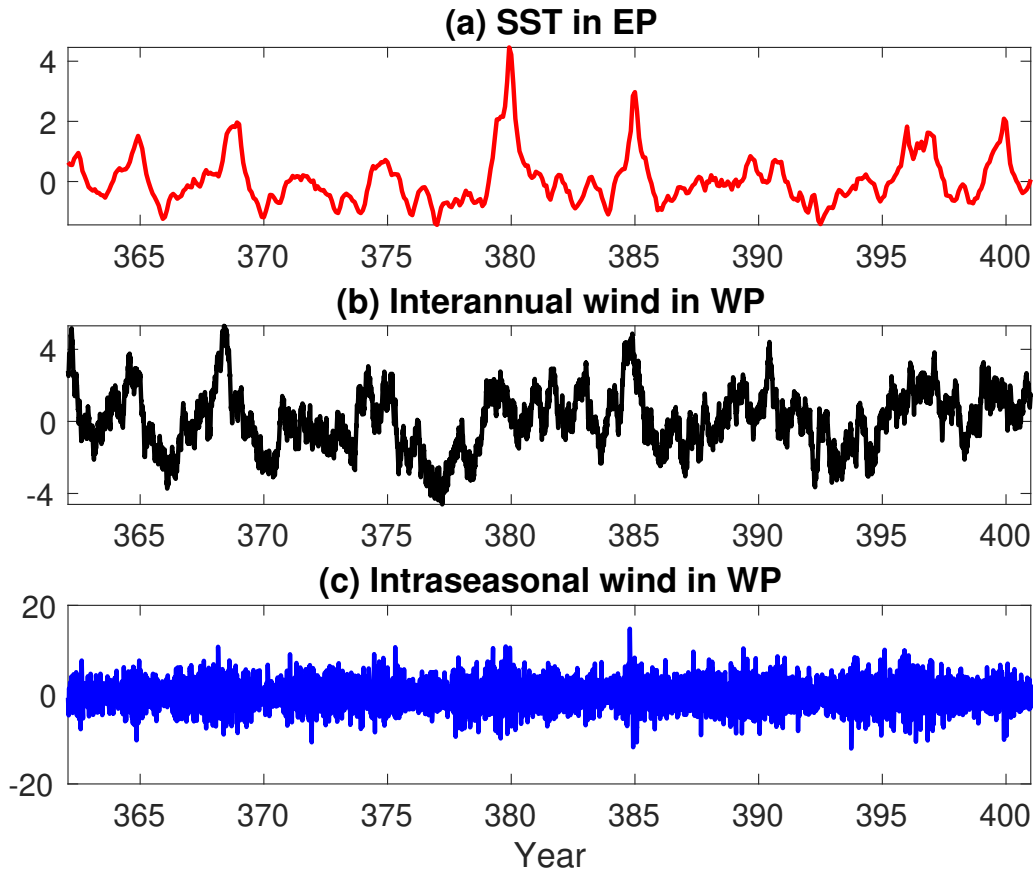


Figure 6.6: Model simulation comparing SST in the EP (T_E) with the two wind components in the WP: the interannual wind (\bar{u}_M) and the intraseasonal wind (u_W).

Karumuri Ashok, Swadhin K Behera, Suryachandra A Rao, Hengyi Weng, and Toshio Yamagata. El Niño Modoki and its possible teleconnection. *Journal of Geophysical Research: Oceans*, 112(C11), 2007.

Hsun-Ying Kao and Jin-Yi Yu. Contrasting eastern-Pacific and central-Pacific types of ENSO. *Journal of Climate*, 22(3):615–632, 2009.

Jin-Soo Kim, Kwang-Yul Kim, and Sang-Wook Yeh. Statistical evidence for the natural variation of the central pacific el niño. *Journal of Geophysical Research: Oceans*, 117(C6), 2012.

Narasimhan K Larkin and DE Harrison. Global seasonal temperature and precipitation anomalies during El Niño autumn and winter. *Geophysical Research Letters*, 32(16), 2005.

Jin-Yi Yu and Hsun-Ying Kao. Decadal changes of ENSO persistence barrier in SST and ocean heat content indices: 1958–2001. *Journal of Geophysical Research: Atmospheres*, 112(D13), 2007.

Jong-Seong Kug, Fei-Fei Jin, and Soon-Il An. Two types of El Niño events: cold tongue El Niño and warm pool El Niño. *Journal of Climate*, 22(6):1499–1515, 2009.

Dake Chen and Mark A Cane. El Niño prediction and predictability. *Journal of Computational Physics*, 227(7):3625–3640, 2008.

Emilia K Jin, James L Kinter, Bin Wang, C-K Park, I-S Kang, BP Kirtman, J-S Kug, A Kumar, J-J Luo, J Schemm, et al. Current status of ENSO prediction skill in coupled ocean–atmosphere models. *Climate Dynamics*, 31(6):647–664, 2008.

Anthony G Barnston, Michael K Tippett, Michelle L L’Heureux, Shuhua Li, and David G DeWitt. Skill of real-time seasonal ENSO model predictions during 2002–11: Is our capability increasing? *Bulletin of the American Meteorological Society*, 93(5):631–651, 2012.

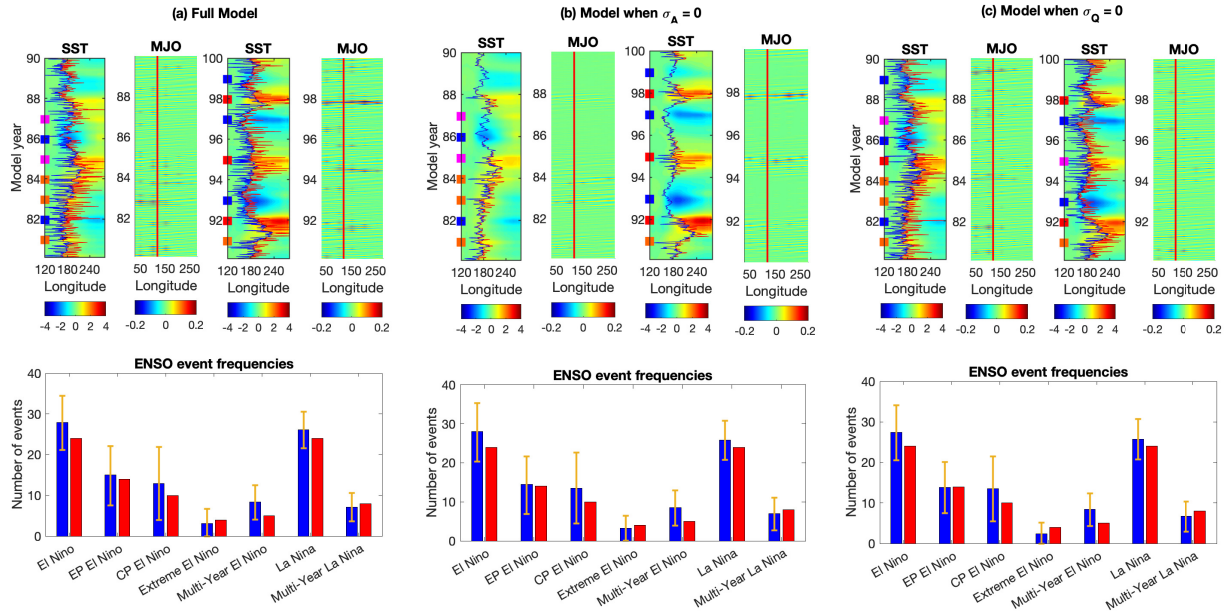


Figure 6.7: Comparison of three model configurations: the full model (Panel (a)), the model without state-dependent noise in A ($\sigma_{\hat{A}_k} = 0$ in (2.3d); Panel (b)), and the model without state-dependent noise in Q ($\sigma_{\hat{Q}_k} = 0$ in (2.3c); Panel (c)). The top row displays Hovmöller diagrams, while the bottom row shows event frequencies over a 70-year period, similar to Panel (f) in Figure 4.1.

Zeng-Zhen Hu, Arun Kumar, Bhaskar Jha, Wanqiu Wang, Bohua Huang, and Boyin Huang. An analysis of warm pool and cold tongue El Niños: Air–sea coupling processes, global influences, and recent trends. *Climate Dynamics*, 38(9):2017–2035, 2012.

Fei Zheng, Xianghui Fang, Jin-Yi Yu, and Jiang Zhu. Asymmetry of the Bjerknes positive feedback between the two types of El Niño. *Geophysical Research Letters*, 41(21):7651–7657, 2014.

Xianghui Fang, Fei Zheng, and Jiang Zhu. The cloud-radiative effect when simulating strength asymmetry in two types of El Niño events using CMIP5 models. *Journal of Geophysical Research: Oceans*, 120(6):4357–4369, 2015.

Soo-Jin Sohn, Chi-Yung Tam, and Hye-In Jeong. How do the strength and type of ENSO affect SST predictability in coupled models. *Scientific Reports*, 6(1):1–8, 2016.

Agus Santoso, Harry Hendon, Andrew Watkins, Scott Power, Dietmar Dommenges, Matthew H England, Leela Frankcombe, Neil J Holbrook, Ryan Holmes, Pandora Hope, et al. Dynamics and predictability of El Niño–Southern Oscillation: an Australian perspective on progress and challenges. *Bulletin of the American Meteorological Society*, 100(3):403–420, 2019.

Jakob Bjerknes. Atmospheric teleconnections from the equatorial pacific. *Monthly Weather Review*, 97(3):163–172, 1969.

Chidong Zhang. Madden-Julian oscillation. *Reviews of Geophysics*, 43(2), 2005.

Steven J Woolnough. The Madden-Julian oscillation. In *Sub-seasonal to seasonal prediction*, pages 93–117. Elsevier, 2019.

C Zhang, ÁF Adames, B Khouider, B Wang, and D Yang. Four theories of the Madden-Julian oscillation. *Reviews of Geophysics*, 58(3):e2019RG000685, 2020.

Youmin Tang and Bin Yu. MJO and its relationship to ENSO. *Journal of Geophysical Research: Atmospheres*, 113(D14), 2008.

Michael J McPhaden, Xuebin Zhang, Harry H Hendon, and Matthew C Wheeler. Large scale dynamics and MJO forcing of ENSO variability. *Geophysical research letters*, 33(16), 2006b.

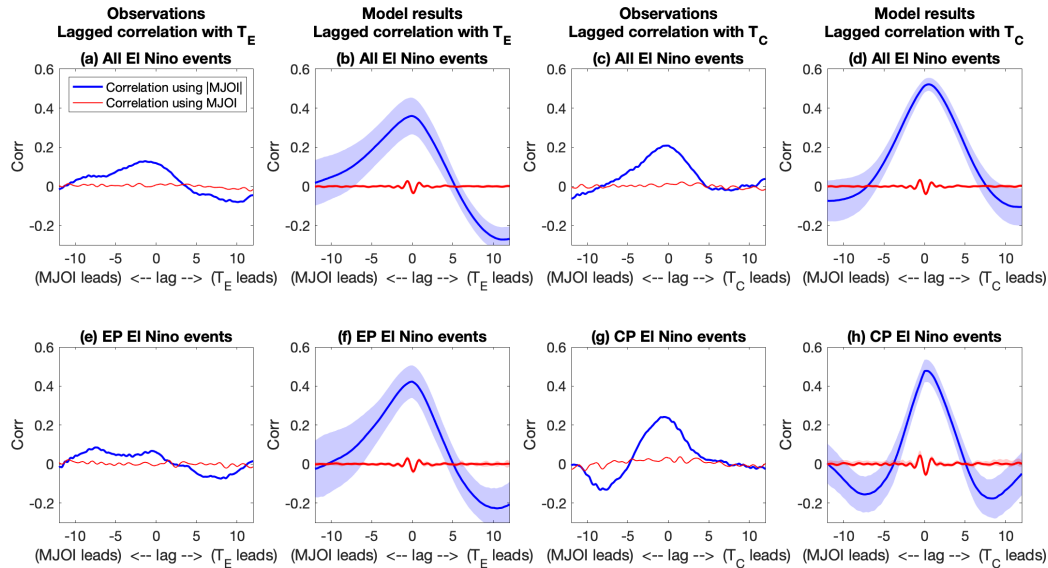


Figure 6.8: Lagged correlation between the MJO and ENSO, similar to Figure 4.3, but for the system with no state-dependent noise in the convective activity equation ($\sigma_{\hat{A}_k} = 0$).

Harry H Hendon, Matthew C Wheeler, and Chidong Zhang. Seasonal dependence of the MJO–ENSO relationship. *Journal of Climate*, 20(3):531–543, 2007.

Martin Puy, Jérôme Vialard, Matthieu Lengaigne, and Eric Guilyardi. Modulation of equatorial pacific westerly/easterly wind events by the madden–julian oscillation and convectively-coupled rossby waves. *Climate Dynamics*, 46(7):2155–2178, 2016.

Martin Puy, Jérôme Vialard, Matthieu Lengaigne, Eric Guilyardi, Pedro N DiNezio, Aurore Voltaire, Magdalena Balmaseda, Gurvan Madec, Christophe Menkes, and Michael J McPhaden. Influence of westerly wind events stochasticity on El Niño amplitude: The case of 2014 vs. 2015. *Climate Dynamics*, 52:7435–7454, 2019.

Yakelyn R Jauregui and Shuyi S Chen. MJO-induced warm pool eastward extension prior to the onset of El Niño: Observations from 1998 to 2019. *Journal of Climate*, 37(3):855–873, 2024.

DE Harrison and Gabriel A Vecchi. Westerly wind events in the tropical pacific, 1986–95. *Journal of Climate*, 10(12):3131–3156, 1997.

Gabriel A Vecchi and DE Harrison. Tropical pacific sea surface temperature anomalies, el niño, and equatorial westerly wind events. *Journal of Climate*, 13(11):1814–1830, 2000.

Eli Tziperman and Lisan Yu. Quantifying the dependence of westerly wind bursts on the large-scale tropical Pacific SST. *Journal of Climate*, 20(12):2760–2768, 2007.

Ja-Yeon Moon, Bin Wang, and Kyung-Ja Ha. ENSO regulation of MJO teleconnection. *Climate dynamics*, 37:1133–1149, 2011.

Robert W Lee, Steven J Woolnough, Andrew J Charlton-Perez, and Frederic Vitart. ENSO modulation of MJO teleconnections to the north atlantic and europe. *Geophysical Research Letters*, 46(22):13535–13545, 2019.

Chalachew Kindie Mengist and Kyong-Hwan Seo. How long can the MJO be predicted during the combined phases of ENSO and QBO? *Geophysical Research Letters*, 49(8):e2022GL097752, 2022.

Xiangwen Liu, Tongwen Wu, Song Yang, Tim Li, Weihua Jie, Li Zhang, Zaizhi Wang, Xiaoyun Liang, Qiaoping Li, Yanjie Cheng, et al. MJO prediction using the sub-seasonal to seasonal forecast model of Beijing climate center. *Climate Dynamics*, 48:3283–3307, 2017.

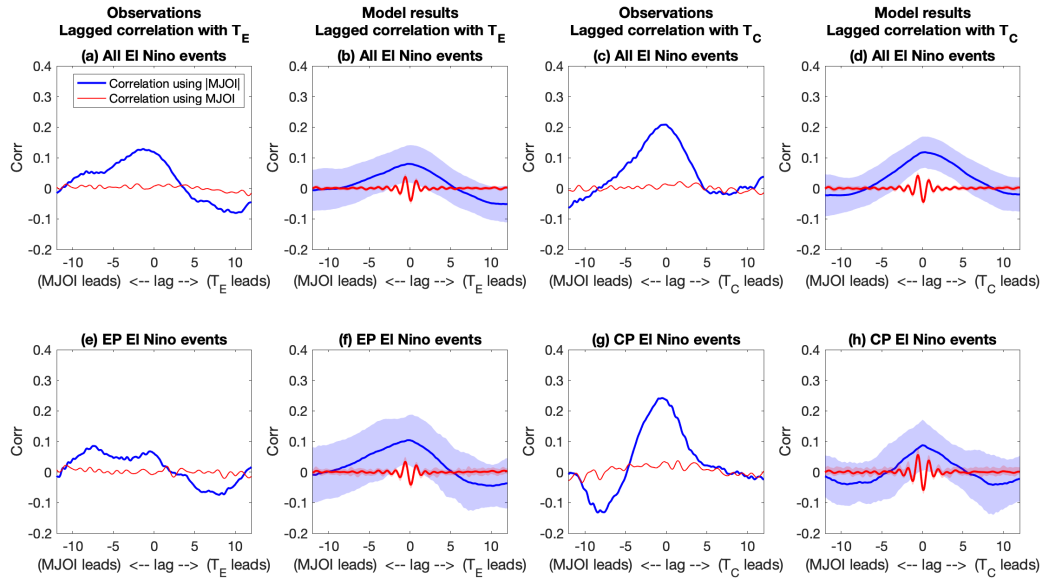


Figure 6.9: Lagged correlation between the MJO and ENSO, similar to Figure 4.3, but for the system with no state-dependent noise in the low-level moisture equation ($\sigma_{\hat{Q}_k} = 0$).

Min-Seop Ahn, Daehyun Kim, Kenneth R Sperber, In-Sik Kang, Eric Maloney, Duane Waliser, Harry Hendon, and WGNE MJO Task Force. MJO simulation in CMIP5 climate models: MJO skill metrics and process-oriented diagnosis. *Climate Dynamics*, 49:4023–4045, 2017.

Meng-Pai Hung, Jia-Lin Lin, Wanqiu Wang, Daehyun Kim, Toshiaki Shinoda, and Scott J Weaver. MJO and convectively coupled equatorial waves simulated by CMIP5 climate models. *Journal of Climate*, 26(17):6185–6214, 2013.

Laís G Fernandes and Alice M Grimm. ENSO modulation of global MJO and its impacts on South America. *Journal of Climate*, 36(22):7715–7738, 2023.

Boualem Khouider, Amik St-Cyr, Andrew J Majda, and Joseph Tribbia. The MJO and convectively coupled waves in a coarse-resolution GCM with a simple multcloud parameterization. *Journal of the Atmospheric Sciences*, 68(2):240–264, 2011.

RS Ajayamohan, Boualem Khouider, and Andrew J Majda. Realistic initiation and dynamics of the Madden-Julian oscillation in a coarse resolution aquaplanet GCM. *Geophysical Research Letters*, 40(23):6252–6257, 2013.

Eric Guilyardi, Antonietta Capotondi, Matthieu Lengaigne, Sulian Thual, and Andrew T Wittenberg. ENSO modeling: History, progress, and challenges. *El Niño Southern Oscillation in a changing climate*, pages 199–226, 2020.

Antonietta Capotondi, Andrew T Wittenberg, Jong-Seong Kug, Ken Takahashi, and Michael J McPhaden. Enso diversity. *El Niño Southern Oscillation in a changing climate*, pages 65–86, 2020.

Chen Chen, Mark A Cane, Andrew T Wittenberg, and Dake Chen. ENSO in the CMIP5 simulations: Life cycles, diversity, and responses to climate change. *Journal of Climate*, 30(2):775–801, 2017.

Bastien Dieppois, Antonietta Capotondi, Benjamin Pohl, Kwok Pan Chun, Paul-Arthur Monerie, and Jonathan Eden. ENSO diversity shows robust decadal variations that must be captured for accurate future projections. *Communications Earth & Environment*, 2(1):1–13, 2021.

Antonietta Capotondi. ENSO diversity in the NCAR CCSM4 climate model. *Journal of Geophysical Research: Oceans*, 118(10):4755–4770, 2013.

- Alyssa R Atwood, David S Battisti, Andrew T Wittenberg, WHG Roberts, and Daniel J Vimont. Characterizing unforced multi-decadal variability of ENSO: A case study with the GFDL CM2. 1 coupled GCM. *Climate Dynamics*, 49:2845–2862, 2017.
- Wenping Jiang, Ping Huang, Gang Huang, and Jun Ying. Origins of the excessive westward extension of ENSO SST simulated in CMIP5 and CMIP6 models. *Journal of Climate*, 34(8): 2839–2851, 2021.
- Gen Li, Yuntao Jian, Song Yang, Yan Du, Ziqian Wang, Zhenning Li, Wei Zhuang, Wenping Jiang, and Gang Huang. Effect of excessive equatorial Pacific cold tongue bias on the El Niño–Northwest Pacific summer monsoon relationship in CMIP5 multi-model ensemble. *Climate Dynamics*, 52:6195–6212, 2019.
- Yingfei Fang, James A Screen, Xiaoming Hu, Shuheng Lin, Ned C Williams, and Song Yang. CMIP6 models underestimate ENSO teleconnections in the Southern Hemisphere. *Geophysical Research Letters*, 51(18):e2024GL110738, 2024a.
- Hye-Mi Kim. The impact of the mean moisture bias on the key physics of MJO propagation in the ECMWF reforecast. *Journal of Geophysical Research: Atmospheres*, 122(15):7772–7784, 2017.
- Guiwan Chen, Jian Ling, Yuanwen Zhang, Xin Wang, and Chongyin Li. MJO propagation over the Indian Ocean and Western Pacific in CMIP5 models: Roles of background states. *Journal of Climate*, 35(3):955–973, 2022a.
- Luke A Parsons, Daniel E Amrhein, Sara C Sanchez, Robert Tardif, M Kathleen Brennan, and Gregory J Hakim. Do multi-model ensembles improve reconstruction skill in paleoclimate data assimilation? *Earth and Space Science*, 8(4):e2020EA001467, 2021.
- Eviatar Bach and Michael Ghil. A multi-model ensemble Kalman filter for data assimilation and forecasting. *Journal of Advances in Modeling Earth Systems*, 15(1):e2022MS003123, 2023.
- Yian Chen and Samuel N Stechmann. Multi-model communication and data assimilation for mitigating model error and improving forecasts. *Chinese Annals of Mathematics, Series B*, 40:689–720, 2019.
- Fei-Fei Jin. An equatorial ocean recharge paradigm for ENSO. Part I: Conceptual model. *Journal of the Atmospheric Sciences*, 54(7):811–829, 1997.
- Paul S Schopf and Max J Suarez. Vacillations in a coupled ocean–atmosphere model. *Journal of Atmospheric Sciences*, 45(3):549–566, 1988.
- Chunzai Wang, Clara Deser, Jin-Yi Yu, Pedro DiNezio, and Amy Clement. El Niño and southern oscillation (ENSO): a review. *Coral reefs of the eastern tropical Pacific: Persistence and loss in a dynamic environment*, pages 85–106, 2017.
- Chunzai Wang and Joël Picaut. Understanding ENSO physics—A review. *Earth’s Climate: The Ocean–Atmosphere Interaction, Geophys. Monogr*, 147:21–48, 2004.
- Julian P McCreary. A model of tropical ocean-atmosphere interaction. *Monthly Weather Review*, 111(2):370–387, 1983.
- Robert H Weisberg and Chunzai Wang. A western Pacific oscillator paradigm for the El Niño–Southern Oscillation. *Geophysical Research Letters*, 24(7):779–782, 1997.
- Joël Picaut, Mansour Ioualalen, Christophe Menkès, Thierry Delcroix, and Michael J McPhaden. Mechanism of the zonal displacements of the pacific warm pool: Implications for ENSO. *Science*, 274(5292):1486–1489, 1996.
- Chunzai Wang. A unified oscillator model for the El Niño–Southern Oscillation. *Journal of Climate*, 14(1):98–115, 2001.
- Nan Chen and Yinling Zhang. Rigorous derivation of stochastic conceptual models for the El Niño–Southern Oscillation from a spatially-extended dynamical system. *Physica D: Nonlinear Phenomena*, 453:133842, 2023.

- Nan Chen, Xianghui Fang, and Jin-Yi Yu. A multiscale model for el niño complexity. *npj Climate and Atmospheric Science*, 5(1):1–13, 2022b.
- Tao Geng, Wenju Cai, and Lixin Wu. Two types of ENSO varying in tandem facilitated by nonlinear atmospheric convection. *Geophysical Research Letters*, 47(15):e2020GL088784, 2020.
- Xianghui Fang, Henk Dijkstra, Claudia Wieners, and Francesco Guardamagna. A nonlinear full-field conceptual model for ENSO diversity. *Journal of Climate*, 2024b.
- Xianghui Fang and Nan Chen. Quantifying the predictability of enso complexity using a statistically accurate multiscale stochastic model and information theory. *Journal of Climate*, 36(8):2681–2702, 2023.
- Marios Andreou and Nan Chen. Statistical response of ENSO complexity to initial condition and model parameter perturbations. *Journal of Climate*, 37:5629–5651, 2024.
- Yinling Zhang, Nan Chen, Jérôme Vialard, and Xianghui Fang. A physics-informed auto-learning framework for developing stochastic conceptual models for ENSO diversity. *Journal of Climate*, 2024. doi: 10.1175/JCLI-D-24-0092.1.
- Stephen E Zebiak and Mark A Cane. A model El Niño–Southern Oscillation. *Monthly Weather Review*, 115(10):2262–2278, 1987.
- Licheng Geng and Fei-Fei Jin. Enso diversity simulated in a revised cane-zebiak model. *Frontiers in Earth Science*, 10:899323, 2022.
- Licheng Geng and Fei-Fei Jin. Insights into ENSO diversity from an intermediate coupled model. Part I: Uniqueness and sensitivity of the ENSO mode. *Journal of Climate*, 36(21):7509–7525, 2023.
- Nan Chen and Xianghui Fang. A simple multiscale intermediate coupled stochastic model for El Niño diversity and complexity. *Journal of Advances in Modeling Earth Systems*, 15(4):e2022MS003469, 2023.
- Sulian Thual, Andrew J Majda, Nan Chen, and Samuel N Stechmann. Simple stochastic model for El Niño with westerly wind bursts. *Proceedings of the National Academy of Sciences*, 113(37):10245–10250, 2016.
- et. al. Vialard, Jérôme. The El Niño southern oscillation (ENSO) recharge oscillator conceptual model: past achievements, future prospects. *Review of Geophysics*, 2024. Under Revision.
- Sulian Thual, Andrew J Majda, and Samuel N Stechmann. A stochastic skeleton model for the MJO. *Journal of the Atmospheric Sciences*, 71(2):697–715, 2014.
- Antonietta Capotondi, Shayne McGregor, Michael J McPhaden, Sophie Cravatte, Neil J Holbrook, Yukiko Imada, Sara C Sanchez, Janet Sprintall, Malte F Stuecker, Caroline C Ummenhofer, et al. Mechanisms of tropical Pacific decadal variability. *Nature Reviews Earth & Environment*, 4(11):754–769, 2023.
- Scott Power, Matthieu Lengaigne, Antonietta Capotondi, Myriam Khodri, Jérôme Vialard, Beyrem Jebri, Eric Guilyardi, Shayne McGregor, Jong-Seong Kug, Matthew Newman, et al. Decadal climate variability in the tropical Pacific: Characteristics, causes, predictability, and prospects. *Science*, 374(6563):eaay9165, 2021.
- Eli Tziperman, Stephen E Zebiak, and Mark A Cane. Mechanisms of seasonal–ENSO interaction. *Journal of the Atmospheric Sciences*, 54(1):61–71, 1997.
- Karl Stein, Axel Timmermann, Niklas Schneider, Fei-Fei Jin, and Malte F Stuecker. ENSO seasonal synchronization theory. *Journal of Climate*, 27(14):5285–5310, 2014.
- Xianghui Fang and Fei Zheng. Effect of the air–sea coupled system change on the ENSO evolution from boreal spring. *Climate Dynamics*, pages 1–12, 2021.
- Xianghui Fang and Mu Mu. A three-region conceptual model for central Pacific El Niño including zonal advective feedback. *Journal of Climate*, 31(13):4965–4979, 2018.

- Jin-Yi Yu and Seon Tae Kim. Identifying the types of major El Niño events since 1870. *International Journal of Climatology*, 33(8):2105–2112, 2013.
- TA Averina and SS Artemiev. Numerical solution of systems of stochastic differential equations. *Russian Journal of Numerical Analysis and Mathematical Modelling*, 3(4):267–286, 1988.
- Qiu Yang, Andrew J Majda, and Nan Chen. ENSO diversity in a tropical stochastic skeleton model for the MJO, El Niño, and dynamic Walker circulation. *Journal of Climate*, pages 1–56, 2021.
- Nan Chen. *Stochastic methods for modeling and predicting complex dynamical systems: uncertainty quantification, state estimation, and reduced-order models*. Springer Nature, 2023.
- Fei-Fei Jin, L Lin, A Timmermann, and J Zhao. Ensemble-mean dynamics of the ENSO recharge oscillator under state-dependent stochastic forcing. *Geophysical Research Letters*, 34(3), 2007.
- Andrew J Majda and Samuel N Stechmann. The skeleton of tropical intraseasonal oscillations. *Proceedings of the National Academy of Sciences*, 106(21):8417–8422, 2009.
- Andrew J Majda and Samuel N Stechmann. Nonlinear dynamics and regional variations in the MJO skeleton. *Journal of the Atmospheric Sciences*, 68(12):3053–3071, 2011.
- Jian Ling, Chongyin Li, Tim Li, Xiaolong Jia, Boualem Khouider, Eric Maloney, Frederic Vitart, Ziniu Xiao, and Chidong Zhang. Challenges and opportunities in MJO studies. *Bulletin of the American Meteorological Society*, 98(2):ES53–ES56, 2017.
- Crispin Gardiner. *Stochastic methods*, volume 4. Springer Berlin, 2009.
- Nan Chen and Andrew J Majda. Filtering the stochastic skeleton model for the Madden–Julian oscillation. *Monthly Weather Review*, 144(2):501–527, 2016.
- DW Behringer and Yan Xue. Evaluation of the global ocean data assimilation system at NCEP: The Pacific Ocean [dataset]. In *Proc. Eighth Symp. on Integrated Observing and Assimilation Systems for Atmosphere, Oceans, and Land Surface*, 2004.
- Boyin Huang, Peter W Thorne, Viva F Banzon, Tim Boyer, Gennady Chepurin, Jay H Lawrimore, Matthew J Menne, Thomas M Smith, Russell S Vose, and Huai-Min Zhang. Extended reconstructed sea surface temperature, version 5 (ERSSTv5): upgrades, validations, and intercomparisons. *Journal of Climate*, 30(20):8179–8205, 2017.
- Bin Wang, Xiao Luo, Young-Min Yang, Weiyi Sun, Mark A Cane, Wenju Cai, Sang-Wook Yeh, and Jian Liu. Historical change of El Niño properties sheds light on future changes of extreme El Niño. *Proceedings of the National Academy of Sciences*, 116(45):22512–22517, 2019.
- Brant Liebmann and Catherine A Smith. Description of a complete (interpolated) outgoing longwave radiation dataset. *Bulletin of the American Meteorological Society*, 77(6):1275–1277, 1996.
- Eugenia Kalnay, Masao Kanamitsu, Robert Kistler, William Collins, Dennis Deaven, Lev Gandin, Mark Iredell, Suranjana Saha, Glenn White, John Woollen, et al. The NCEP/NCAR 40-year reanalysis project. *Bulletin of the American Meteorological Society*, 77(3):437–472, 1996.
- Samuel N Stechmann and Andrew J Majda. Identifying the skeleton of the Madden–Julian oscillation in observational data. *Monthly Weather Review*, 143(1):395–416, 2015.
- Sulian Thual, Andrew J Majda, and Nan Chen. A tropical stochastic skeleton model for the MJO, El Niño, and dynamic Walker circulation: A simplified GCM. *Journal of Climate*, 31(22):9261–9282, 2018.
- Ángel F Adames and Daehyun Kim. The MJO as a dispersive, convectively coupled moisture wave: Theory and observations. *Journal of the Atmospheric Sciences*, 73(3):913–941, 2016.
- Da Yang and Andrew P Ingersoll. Triggered convection, gravity waves, and the MJO: A shallow-water model. *Journal of the atmospheric sciences*, 70(8):2476–2486, 2013.

- Bin Wang, Fei Liu, and Guosen Chen. A trio-interaction theory for Madden–Julian oscillation. *Geoscience Letters*, 3(1):1–16, 2016.
- Cécile Penland and Prashant D Sardeshmukh. The optimal growth of tropical sea surface temperature anomalies. *Journal of Climate*, 8(8):1999–2024, 1995.
- Andrew M Moore and Richard Kleeman. Stochastic forcing of ENSO by the intraseasonal oscillation. *Journal of Climate*, 12(5):1199–1220, 1999.
- Fei-Fei Jin, Soon-Il An, Axel Timmermann, and Jingxia Zhao. Strong El Niño events and nonlinear dynamical heating. *Geophysical Research Letters*, 30(3):20–1, 2003.
- Soon-Il An and Fei-Fei Jin. Nonlinearity and asymmetry of ENSO. *Journal of Climate*, 17(12):2399–2412, 2004.